A numerical study on turbulence generation and decay in a suddenly stopped Taylor-Couette flow

Pau Manyer Fuertes
Dr. Jose Manuel Lopez Alonso
Dr. Daniel Feldmann

27th June 2022

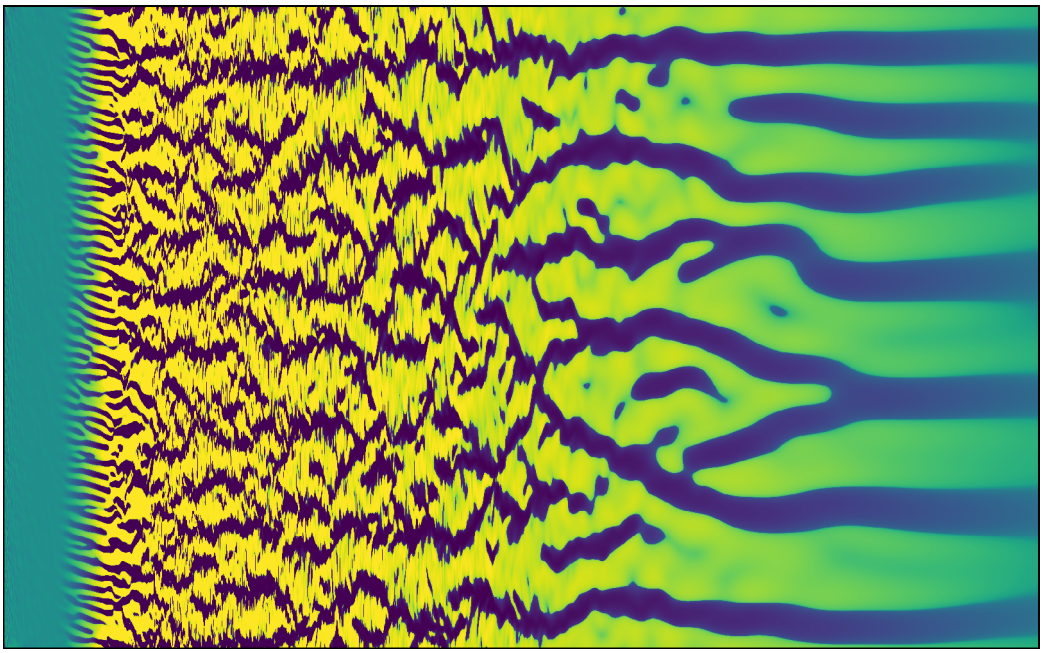

Abstract

Almost every single flow of fluid in the known Universe is turbulent. Hence, it is essential in order to keep moving forward in research and industrial development to obtain accurate ways of modeling turbulence in fluids without depending on DNS, which already nowadays presents limits in terms of computational cost when dealing with high-Re flows in broad spatial domains. Obtaining new insight on turbulent flows might help enhancing the mathematical or computational models for turbulence.

Therefore, the study hereby presents the analysis and results obtained from the numerical simulation of an abruptly stopped Taylor-Couette system, which guarantees both inhomogeneousity and anisotropy of the wall–bounded flow. The simulations are performed using the Fortran code `nsCouette` modified so that the outer cylinder is halted according to a tanh profile. The experimental results are reproduced with great accuracy and new knowledge is brought into light on the generation and free decay of turbulence.

While the inner cylinder remains at rest, rapidly halting the outer one causes the generation of a centrifugal instability zone in the laminar flow near the outer cylinder. Inside the unstable region, axi-symmetrical vortical structures are formed and rapidly grow until filling the whole gap between cylinders. At such point, the vortices are destabilized by secondary instabilities originated by the constant reorganisation of the structures in the gap. The flow transitions then towards turbulence. The turbulent flow enters then a free decay stage since both cylinders are static. Shortly after, the system progressively regains large scale structures while transitioning to a purely viscous decay, with a steeper decay exponent. Hence, this process can be divided into three different stages: generation of turbulent; turbulent free decay; viscous free decay.

The turbulent kinetic energy and the dissipation rate of turbulent kinetic energy are characterised during the free decay of turbulence, for several outer cylinder initial Reynolds number and at different radial locations in the gap. Both magnitudes are fitted according to a power law function and the computed decay exponents are presented for the different cases.

Key words: Taylor–Couette, Reynolds number, turbulence, centrifugal instability, decay.

Acknowledgements

I would like to express my gratitude to Dr. Jose Manuel Lopez Alonso (UPC, Barcelona) and Dr. Daniel Feldmann (ZARM, Bremen) for being my thesis supervisors. I manage to learn a lot from both on how to develop and carry out a research project. Specially, to start working with clusters and parallel coding has been a privilege and I would like to thank Jose and Daniel for helping me out. I would also like to acknowledge the constructive conversations and the good moments I had with Dr. Alberto Vela and Daniel Morón, as well as cheerful welcoming I received at ZARM from the whole Fluid Mechanics research group.

The experience wouldn't have been the same without my new friends from the University campus at *Vortrasse Studentwerk*, my flatmates from D13 and my neighbors from D12.

To all, thank you.

Pau Manyer, Bremen, June 2022

Contents

1. Introduction

1.1 Motivation and background

> *"There is a physical problem that is common to many fields, that is very old, and that has not been solved. [...] Nobody in physics has really been able to analyze it mathematically satisfactorily in spite of its importance to the sister sciences. It is the analysis of circulating or turbulent fluids."*
> — *Richard P. Feynman,* The Feynman Lectures on Physics Vol 1

It is often said that Turbulence is the last unsolved problem in Classical Physics. In fact, nowadays there still exist no theory of turbulence being able to predict the exact statistical behaviour of turbulent flows due to the *Closure Problem*, and mathematical models trying to fill that void have still a long way to go. However, we believe that in order to understand the motivation and the relevance behind the work we will present, we need to take several steps backwards and start from the beginning.

It is a rather common mistake in our society to associate *fluid* with *liquid*. In fact, Fluids can be defined as any substance or entity that can be deformed continuously under an applied external force. This of course encloses inside such term any gaseous as much as any liquid entity, for instance the water in the ocean, the air in the atmosphere, the blood in our veins or even the magma inside the earth. Hence, fluids are to be found everywhere in the known Universe, being intrinsic to life itself.

Now, when external forces are applied, fluids will deform and move: that is what we would call *flow* of the fluid. The study of fluid's flows is at the core of Fluid Mechanics, nonetheless it transcends to almost every branch of Physics. However, after decades of study and experimentation very little is known about the subject and no theory can hope to describe all flows of fluid, at least turbulent ones. A fluid flow can be categorised as *laminar* or *turbulent*.

Laminar fluid flows, or streamline move in parallel "layers" and have minimal lateral mixing. In a laminar flow the trajectories do not ever cross. It is an organized movement across space with no interaction between the fluid particles. On the other hand, turbulent flows are described by chaotic movement of the fluid particles. Their trajectories cross, which means there is mixing between layers and interaction between fluid particles. Their velocity in not uniform and depends on time and position, and the presence of struc-

tures we call *eddies* of different sizes is a property of turbulent flows. An eddy can be defined as a blob of vorticity (local spinnig motion) in the fluid. In turbulent flows, this vorticity is carried and translated due to diffusion and advection mechanisms.

As one might guess, studying turbulent flows is way more difficult than laminar ones, and at the same time this is a hardship from which we cannot escape due to the fact that almost any known flow of interest in our Universe is turbulent. The air flowing in and out of our lungs is turbulent, as is the natural convection in the room in which you sit. Turbulence controls the drag on cars, aeroplanes, and bridges, it dictates the weather through its influence on large-scale atmospheric and oceanic flows, the terrestrial magnetic field is maintained due to the turbulence in the liquid core of the Earth... Whereas we wish to enhance the industrial applications such as vehicles, aerospace, energy (eolian, nuclear, hydraulic...) or transport (with pipes for instance) or we want to research the physics behind the life of stars or our own, Turbulence will always be waiting for us.

Therefore, the importance of unveiling the mysteries of turbulence is crucial. For fluid flows, be they laminar or turbulent, the governing laws are embodied in the Navier-Stokes equations, which have been known since 1850. The Navier-Stokes equations are a set of differential equations which return the velocity field of the fluid particles in the geometry considered when solved. Considering the diversity and complexity of fluid flows, it is quite remarkable that such simple equations describing the behaviour of such flows exist. Moreover, these equations are deterministic, which means that they can be integrated in time in order to simulate any possible problem set.

Then, if the problem can be solved by integrating the Navier-Stokes equations using numerical methods, why is it that turbulence is still said to be an unsolved problem? Well, the answer must be carefully explained. On one hand, it is true that Navier-Stokes equations describe accurately the behaviour of any fluid flow and therefore direct simulations (DNS) can be used in order to study turbulent flows with great precision. However, on the other hand the DNS that can be run nowadays of real life problems with the computational power we hold are very limited. For instance, we cannot hope to simulate using DNS the air drag around a car for say 10 seconds. It would take months of computation. It seems ironic but the issue resides in the perfect accuracy of the Navier-Stokes equations. As far as turbulent flows are concerned, their power is also their weakness: they describe every detail of the turbulent velocity field from the largest to the smallest length and time scales.

In fact, the chaotic movement in a turbulent flow causes the fluid particles to interact with each other, colliding and rubbing one another, thus exchan-

ging momentum. This local description can be averaged at a bigger scale, seen as shear stress in the fluid, a dragging force between different fluid particles moving at different speed and direction. This viscous shear stress between fluid particles is responsible for the energy dissipation inside the fluid, however this is not true always. What we mean is that the dissipation of kinetic energy into heat by viscous shear stress is only possible if the viscous forces are comparable to the inertial forces locally. Otherwise, turbulence acts just as a mechanism to redistribute linear momentum. Hence, we encounter a necessary condition for turbulence to dissipate energy: both inertial forces and viscous forces must be comparable.

In terms of the addimentional parameter known as Reynolds number Re, this condition can be translated as $Re \sim 1$. The Reynolds number represents the ratio between the inertial forces and the viscous ones, defined as $Re = uL/\nu$ where u is the flow velocity, L is a characteristic length of the system and ν is the viscosity. Then, generally, high–Re flows tend to be turbulent ones because the inertial forces are orders of magnitude larger than the viscous ones.

Therefore, the question is now to know when this condition is met. Well, physicists realised from the beginning that turbulent flows, at any instant, presented a broad spectrum of eddy sizes. It turns out that, after thorough studies, the condition is satisfied when considering locally the smallest eddies of the spectrum, thus meaning that the dissipation of kinetic energy within a turbulent flow is located at such (small) scales. These observations led to the concept of *Energy Cascade* for highly turbulent flows.

The idea is the following. The largest eddies, which are created by the instabilities in the mean flow, are themselves subject to inertial instabilities and rapidly "break-up", transferring their kinetic energy progressively via stretching of the turbulent eddies, into smaller vortices. Of course, the smaller eddies are themselves unstable and they, in turn, pass their energy onto even smaller eddies, and this hierarchy is carried on. Thereby, at each instant, there is a *cascade* of energy from the large turbulent structures to the small ones. The process comes then to a halt at certain small scales, when the viscous forces are strong enough (comparable to the inertial forces) to dissipate the kinetic energy into heat through viscous shear stress. From here, the cascade starts once again from the beginning and will carry on as long as flow presents a source of energy (pressure gradient, mechanical work...) for the mean flow and perturbations to generate turbulent instabilities.

Furthermore, as one walks down the cascade, the transfer of energy from larger eddys to smaller ones becomes faster. This means that higher-turbulent viscous processes will be characterised by lower length and time scales. In fact, this knowledge is still nowadays the burial stone for DNS

methods in Fluid Mechanics and answers our previous intrigue on the importance of scales. One might then say that the problem could be solved using a less precise grid and then expecting approximated solutions, but in fact if the smallest scales are not computed in a turbulent flow, the solution is just wrong. The dissipation of energy and the cascade is cut-off, meaning that the whole cycle is incomplete. Risking failure of expensive projects due to wrong simulation results is not a option.

Therefore, we find ourselves in front of a paradox: although we possess the deterministic Navier-Stokes equations which predict the exact behaviour of turbulent flows, we cannot use DNS to integrate the equations because we lack computational power to simulate all the necessary scales from high-turbulence flows, which are precisely the kind of flows one finds in the Universe and industrial applications.

Hence, as they say, when a door closes another one opens. It is well known that Navier-Stokes equations are highly non-linear and therefore describe phenomena that rapidly becomes chaotic. Nonetheless, physicists noticed that, similarly to the study of gas molecules, while it is impossible to predict the individual features of every single fluid element, the global outcome of the whole system may be predicted statistically. That is, just as in the kinetic theory of gasses, one might be able to average the apparently random motion of individual fluid particles and produce a non-random, macroscopic, statistical model.

However, once again physicists stumbled upon a new issue: the Closure Problem of Turbulence. In fact, when manipulating the time-averaged Navier-Stokes equations in the search of dynamical equations for the statistical quantities of the flow, new crossed quadratic terms appear, descendants of the non-linear term in the original equations. This couples the mean flow to the turbulent one, and therefore one needs to yield some knowledge on the turbulence, which is chaotic and random, in order to predict the behaviour of the mean flow. There is no way obtaining closed dynamical equations for the crossed-terms and therefore entering a statistical description of turbulence demands the ultimate price: there are always more unknowns than equations.

Turning back to a deterministic approach is not possible though, so the only way forward is to deal somehow with the closure problem. To close the system some additional information must be introduced, necessarily *ad hoc* in nature.

For almost a century, engineers have plugged this gap using the eddy-viscosity hypothesis and, indeed, this still forms the backbone for many engineering models of turbulence. The hypothesis is a very simple one: due to the turbulence in the flow and the generation of eddies in a vast spec-

trum of sizes, the viscosity of the fluid increases. Today, the most common model used in computation fluid dynamics, industrially, in aerospace, vehicles, chemistry... is the so called $k - \varepsilon$ turbulence model. That is, the Reynolds-Averaged Navier-Stokes (RANS) equations, which are the dynamical equations for statistical quantities in the flow, combined with the equations from the $k - \varepsilon$ turbulence model.

The model assumes that the eddy viscosity ν_t can be expressed as $\nu_t = C_\nu \cdot k^2/\varepsilon$ where k is the turbulent kinetic energy, ε is the rate of dissipation of turbulent kinetic energy and C_ν is a constant to be determined. Furthermore, two additional transport equations (which are partial differential equations) describing the dynamics of k and ε give a general description of the turbulence. In fact, the standard $k - \varepsilon$ turbulence model introduces several constants yielded in the transport equation for the decay rate ε. However, such constants cannot be mathematically obtained, but instead must be fitted from experimental or numerical data. This is precisely the reason why researchers and engineers are interested in free decay of turbulent flows. Learning and analysing why, when and how turbulence decays freely yields the key to better fitting and improve models, which means better, faster, and more accurate results using numerical simulations. This in turn means more efficient and improved industrial applications that will, we hope, result in substantial benefits for our society.

1.2 State of the art

A first approach to study the free decay of turbulence in fluid flows was undertaken in the frame of homogeneous isotropic turbulence (HIT). Nonetheless, real turbulence is neither homogeneous nor isotropic, but instead is highly chaotic, shows no isotropy and often is wall-bounded, with a considerable fraction of the dissipation in the fluid taking place in the corresponding boundary layers. Several studies have been made during the last decades, either experimental or numerical, in different wall-bounded geometries such as pipes flows (Peixinho & Mullin 2006 [1]), two plates distributions (Touil *et al.* 2002 [2]) or Taylor-Couette (TC) (Verschoof *et al.* 2016 [3]; Ostilla-Mónico *et al.* 2017 [4]) systems which consists of a fluid confined between two concentric cylinders. Pipes present a lot of difficulties when studied experimentally due to the translation of the decaying turbulent flow being flushed away downstream. However, this problem is non existing when working with a TC system, which guarantees at the same time the turbulent flow to be neither homogeneous nor isotropic. Moreover, both experimentally and numerically, the TC system can be studied without using a very big apparatus,

its modest size offers a more practical way to investigate turbulence decay in wall-bounded structures.

All in all, we can argue that the Taylor–Couette system is a very good way to research turbulence decay. On one hand, Verschoof *et al.* 2016 [3] described the results obtained when studying in a TC system the decay of turbulent flow generated when rotating the inner cylinder (the outer cylinder was at rest), and compares it with the results predicted by the HIT model. In the experiment, using non-intrusive optical methods the researchers are able to measure the velocity of the fluid particles in the flow, and from that compute both turbulent kinetic energy k and energy dissipation rate ε. However, this set-up presented some practical problems when stopping the cylinder, which took 12 seconds to halt completely. During this time, measurements couldn't be realised and therefore the first stages of turbulence decay, which are the most important and significant ones, couldn't be observed. This experimental study was followed by a numerical one by Ostilla-Mónico *et al.* 2017 [4].

By rotating the inner cylinder in a TC system (while keeping the outer cylinder at rest), if Re is high enough the flow becomes rapidly turbulent. Then, when the inner cylinder is stopped abruptly, the input supply of energy to the system is cut-off allowing to study how the turbulent flow decays with time. Nonetheless, in real life the term "abruptly" does not mean "instantaneously", as this would be physically impossible. This is a problem because the measurements performed while the cylinder is stopping are in fact not for "free decay", as the system is still receiving an energy input from the rotating cylinder. Hence only measurements realised when the cylinder is completely at rest are valid to study free-decay turbulence, which is the main goal of the experiment. Furthermore, as one increases Re, which in the TC system means increasing the speed at which the cylinder rotates, the time necessary to stop the cylinder increases. That is, the results obtained for more realistic turbulent flows, which are high-Re, are less exploitable because the earliest stages of the decay are completely altered by the energy input. Hence, clearly this experiment is not optimal to study free decay turbulence.

A new approach is undertaken by H. Singh and A. Prigent (2021) [5], which presents a slightly different methodology respect to the one discussed earlier: in this case, it is the outer cylinder in the TC that is rotated and abruptly stopped, while the inner cylinder remains at rest. In the TC system, turbulence cannot be generated if only the external cylinder is rotating: the flow remains laminar despite the value of Re. However, by abruptly stopping the external cylinder one changes radically the flow's boundary conditions, which causes a large instability that, if Re is high enough, rapidly turns into turbulence. This turbulence, as both cylinders are at rest, the flow can decay

freely, without any external input of energy. Hence, this new experiment is optimal for our purposes, and even shows us more than we expected: researchers are able not only to study free decay of turbulent flows, but also to observe its generation.

This whole process has been described in the DNS by Kaiser *et al.* (2020) [6], but in this case for a simple cylinder containing fluid which is rotated and then abruptly stopped. This can be considered a particular case of the TC system where the radius ratio is $\eta = r_i/r_o = 0$ (where r_i and r_o are the radius for the inner and outer cylinders respectively). H. Singh and A. Prigent (2021) [5] often compare their experimental results to the ones obtain by Kaiser *et al.* (2020) [6].

Nonetheless, our attention is driven towards the experimental results presented in [5]. The first results described by these authors are purely descriptive, showing how shortly after the external cylinder is stopped, small vortical structures start developing near the outer wall and grow progressively towards the inner cylinder, ultimately filling all the gap of the system. This process is represented using several visualisations of the cross-section gap between the cylinders at different instants of time in the form of binarized instantaneous images, as one may see in figure 1.1.

This is indeed the very first figure presented in [5]. Further in the paper, the description and analysis of the whole phenomena, from the abruptly stoppage until the recovery of laminar regime, is supported by the representation of several space-time diagrams at mid-gap for different values of Re_o, the outer cylinder's initial Reynolds number, defined as $Re_o = u_i r_o/\nu$ (where the u_i is the initial rotation velocity of the outer cylinder). In fact, 3 different phases can be identified during the process: after the cylinder is stopped, vortical structure appear and grow until filling the whole gap and then, due to secondary instabilities, these structures are destabilised and lead to a turbulent regime (phase I); shortly after the generation and growth of turbulence, the disturbed flow starts decaying freely, the whole gap being filled with turbulence with a constant reorganisation of the structures and the lengths scales (phase II); finally, the biggest structures formed by the reorganisation process disappear progressively following a purely viscous decay (phase III). Furthermore, the higher the initial Re_o value is, the faster the vortices appear throughout the axial length and the longer the turbulent phase last. In viscous time units, the time required by the vortices to fill up the gap width decreases with each increment in Re_o, and the growth can be well approximated by a power law fit $\sim t^{\xi}$ with exponent $\xi = 0.5$ when plotted against the time. It was speculated that he size of the vortical structures is also associated to the unstable zone originated by a centrifugal instability in the system, due to the abrupt stoppage of the outer cylinder.

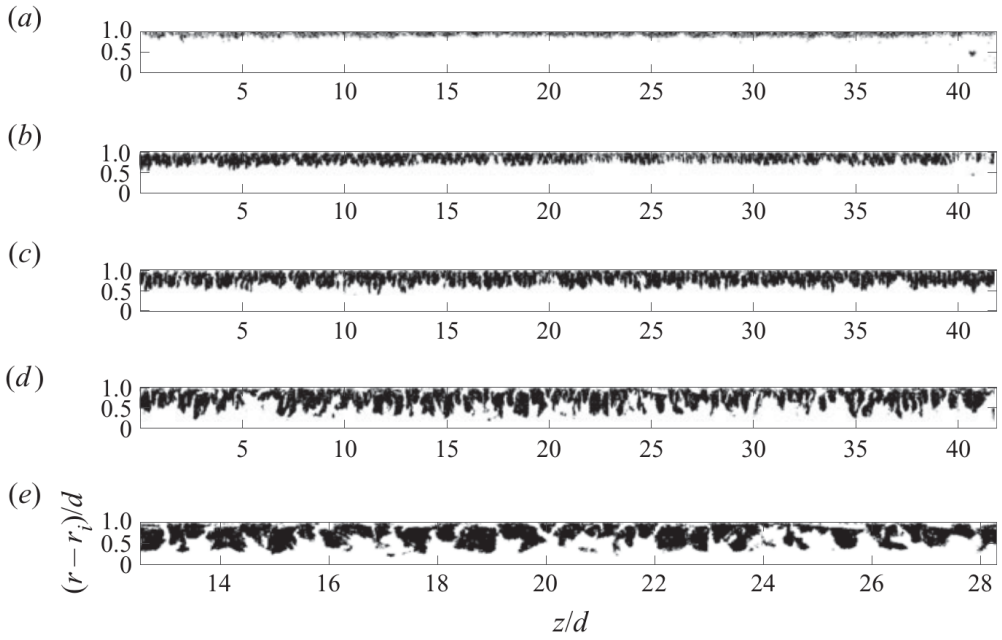

Figure 1.1: Generation and growth of turbulent eddies in an abruptly stopped experimental Taylor–Couette flow. Several binarized instantaneous images are exhibited presenting the growth of vortical structures at different times steps for $Re_o = 1700$ over the whole axial height (z) of the TC system. The x and y labels are the same for all panels as in (e): (a) $t = 0t\nu/d^2$; (b) $t = 0.005t\nu/d^2$; (c) $t = 0.01t\nu/d^2$; (d) $t = 0.017t\nu/d^2$; and (e) $t = 0.017t\nu/d^2$ with zoom. Figure taken from [5].

The unstable region appears near the outer cylinder and then grow towards the inner one.

Moving forward in [5], it is also shown that the instant at which decay starts is the point of stoppage as well, basing the explanation on the decaying behaviour of the azimuthal velocity radial profile along the gap. This profile is also used to study the unstable zone where the vortices appear, between its maximum value u_θ and the outer cylinder's wall.

Afterwards, the discussion turns directly towards the decay of kinetic energy and energy dissipation rates. In general, the behaviour of the three characteristic measurements of kinetic energy, k_{mean}, k_{turb} and k_{wind}, is the same independently of the initial Re_o. It can also be seen that while the mean kinetic energy is constantly decaying, both turbulent and wind components present a growth followed by decay stages. This supports further the idea of a triphasic process explained earlier. The same behaviour is observed for the turbulent dissipation rate ε_{turb} and for the production of kinetic energy P. However, no fitting could be performed on ε_{turb} during the turbulent free decay phase due to the presence of oscillations in the profile. An analysis on the profiles for the Taylor microscale λ and for the Kolmogorov scale η_K show that λ describes better the energy decay and should be considered the length scale for phases I and II.

Finally, a self-similarity study on the radial profile for the azimuthal velocity at $Re_o = 17300$ for the decaying phases is undertaken, normalizing the profile with its spatial average based on [3]. Self-similar profiles are observed during the turbulent decay phase.

1.3 Research questions

Hence, those were the results obtained by H.Singh and A.Prigent (2021) in [5] during the experiments they performed in a TC system. Nonetheless, it is pointed out at the end of the paper: *"An experimental analysis would be most welcome but a numerical approach can definitely present some new ideas."* This is precisely the point where we resume the study in this framework.

The goal of this document is to carry out a study of the same system and the same scenario, but numerically. We wish to see if the same results obtained experimentally can be generated using numerical simulations, and if so, if the outcome can offer new insight into the nature of turbulence generation and, most importantly, free decay in wall-bounded flows.

Numerical methods offer a vast collection of advantages respect to experimental procedures. All magnitudes that would experimentally depend on the precision of the instrument of measure are now computed with greater

accuracy, at every point in the numerical grid. Furthermore, obtaining data near the walls, both of the inner and outer cylinder, is no longer a problem: data is accessible at every point of the grid. The results presented in [5] did not take into account the azimuthal dependence of the flow, as this could not be determined with experimental measurements. The data was smoothed by averaging over the axial direction and in time. However, temporal averaging in a transient problem is not a good *praxis*. In numerical simulations the data can be averaged spatially in both azimuthal and axial directions. This allows us to obtain smooth data at each time instant, avoiding the necessity of temporal averaging.

Moreover, numerical methods may be the key to studying the turbulence in this problem at higher Reynolds values. For instance, the highest Re_o presented in [5] is $Re_o = 17300$, thus of the order of 10^4. Numerically, with enough computational power, studies of the order of $Re \sim 10^5$ could be performed.

Hence, the guideline to be followed is the study on turbulence performed by H. Singh and A. Prigent (2021) in [5]. In what follows, we define the key questions addressed in the present study:

- Can we reproduced the experimentally observed flow phenomena in a numerical simulations of the Taylor–Couette flow with a stopping outer cylinder?
- Is the generation and growth of the observed vortical structures related to the classical centrifugal instability?
- Can we characterise the free decay of inhomogeneous and anisotropic turbulence in a wall-bounded flow with respect to the Reynolds number (driving speed) and to the inhomogeneous radial direction of the system?

2. Methodology

2.1 Taylor-Couette system & Navier-Stokes equations

Figure 2.1 **a)** presents the well–known Taylor–Couette system used by H. Singh and A. Prigent (2021) to perform their experiments in [5] and by us in our numerical simulations. The system is formed out of two coaxial cylinders, an inner cylinder and an outer cylinder of radius r_i and r_o respectively. Both cylinders rotate independently from one another, in any sens and at whatever velocity. The gap between cylinder $d = r_o - r_i$ is usually taken as characteristic length unit to turn the magnitudes dimensionless. Figure **b)** on the other hand represents a the cylindrical coordinates system which will be used for this problem, being $\hat{r}$ the radial direction, $\hat{\theta}$ the azimuthal direction and $\hat{z}$ the axial direction.

The governing equations of the problem are the incompressible Navier-Stokes equations, that is equations 2.1 and 2.2, where $\mathbf{u} = \mathbf{u}(r, \theta, z, t) = (u_r, u_\theta, u_z)$ is the velocity field of the flow. u_r, u_θ and u_z are respectively the radial, azimuthal and axial components of $\mathbf{u}$. $p = p(r, \theta, z, t)$ is the pressure, while ρ and ν are the density and viscosity of the fluid respectively, both constants.

$$\frac{\partial \mathbf{u}}{\partial t} + (\mathbf{u} \cdot \nabla)\mathbf{u} = -\frac{1}{\rho}\nabla p + \nu \nabla^2 \mathbf{u} \tag{2.1}$$

$$\nabla \cdot \mathbf{u} = 0 \tag{2.2}$$

2.2 nsCouette

We will use the code known as `nsCouette` (open source, may be found in `GitHub`).

It is a highly scalable software tool to solve the Navier–Stokes equations for incompressible fluid flow between differentially heated and independently rotating, concentric cylinders (TC system) [7]. It is based on a pseudospectral spatial discretization and dynamic time-stepping. That is, on one hand, the Navier-Stokes equations are discretized using a pseudospectral Fourier—Galerkin ansatz for the $\hat{\theta}$ and $\hat{z}$ directions while in $\hat{r}$ (the only inhomogeneous direction due to the use of a Chebyshev gridding for $\hat{r}$) high-order explicit finite differences are used. On the other hand, the temporal integration scheme is based on a predictor-corrector method [8]. This enables a variable time-step size with dynamic control, which is of advantage if the flow state is

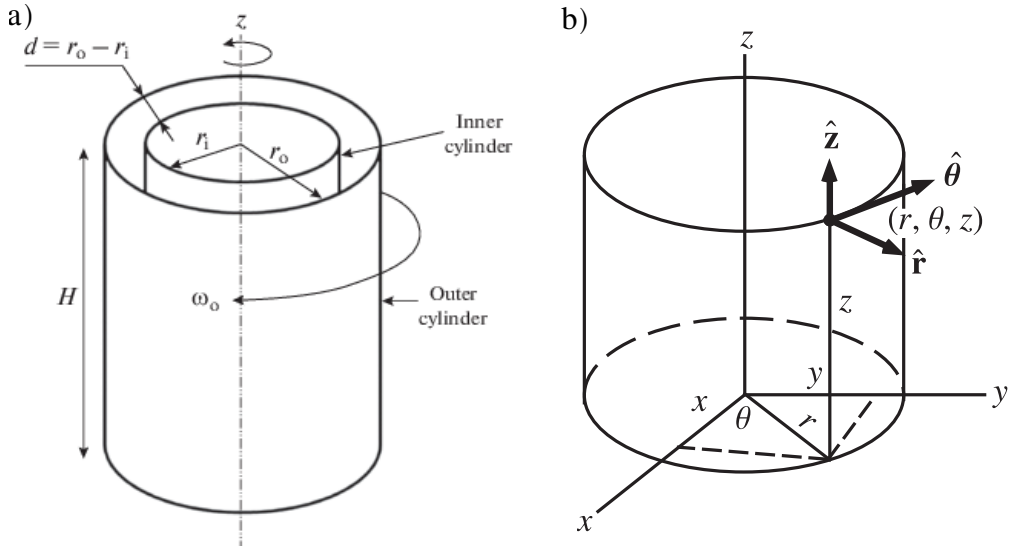

Figure 2.1: **a)** Scheme of a Taylor-Couette system ; **b)** Cylindrical coordinates system.

either suddenly modified (as is the case in our study) or naturally undergoes strongly transient dynamics. It is implemented in modern `Fortran` with a hybrid `MPI-OpenMP` parallelization scheme [9] and thus designed to compute turbulent flows at high Reynolds.

Periodic boundary conditions are assumed in $\hat{z}$, thereby avoiding the need for dense grids close to the vertical boundaries. Note, that the comparison between DNS with axially periodic boundary conditions and laboratory experiments with solid end-plates is extremely satisfactory for a wide range of Re ranging from laminar to highly turbulent flows in the ultimate regime [10].

In `nsCouette` the Fourier coefficients and optionally also the primitive variables are dumped to individual files for each time step at user-specified output intervals. It also implements an easy-to-use checkpoint-restart mechanism based on the Fourier-coefficients for handling long-running DNS. The primitive variables – velocity (u_r, u_θ, u_z), pressure (p) and optionally temperature (T) – are written in `HDF5` format, along with metadata in a small `xdmf` file in order to facilitate analysis with common visualization tools like `ParaView` and `VisIt`.

`nsCouette` uses a single input file to define all relevant parameters (number of points, modes and time steps, rotation rates etc.) at program startup. At every restart, the spatial resolution can be freely changed using an auto-

mated interpolation and mode padding functionality.

However, the original `nsCouette` that one may find and download in the `GitHub` repository was not designed for the experiment we want to reproduce. That is, the source code doesn't implement "outer cylinder stopping". Hence, the first step of our project was to generate a `Fortran` subroutine in the `nsCouette` code in order to stop the initially rotating outer cylinder of the TC system.

The subroutine that implements this functionality is referred in the code as `OuterReynolds`. It is based on 5 new parameters that control the features of the stoppage process, 4 of them needing to be specified in the input file defining all relevant parameters. `re_o_initial` is a constant which takes the value of the initial Reynolds number of the outer cylinder Re_o at the beginning of the simulation (this is the parameter which is not contained in the input file, as it automatically takes the value given to the input file variable `Re_o`); `t_stop` yields the instant (in viscous units of time) at which the stopping of the outer cylinder will begin; `tau_stop` yields the duration (in viscous units of time) of the stopping process; `real_stop` is a boolean parameter yielding how the stopping process will be carried on, that is whether Re_o will be following a linear decrease (when `real_stop` = False) or a tanh decrease (when `real_stop` = True). The implementation of a tanh is motivated by the need to reproduce a real mechanical activator response, that is the stopping process of the outer cylinder rotation will be triggered by a mechanical or electronic device generating a response in the system. Therefore, when `real_stop` = True, Re_o will be following a function such as

$$Re_o(t) = Re_o^{initial} \cdot \frac{1}{2}\left[\tanh\left(-\frac{t-t_0}{\beta}\right)+1\right] \quad \text{where} \quad \begin{cases} t_0 = t_{stop} + \frac{1}{2}\tau_{stop} \\ \beta = \frac{\tau_{stop}}{\ln\left(\frac{1}{\epsilon}-1\right)} \end{cases}$$

with the auxiliary parameters t_0 corresponding to the instant when the stopping process is half-way, β yielding the slope of the tanh and ϵ being the percentage of error of the value of the function at the boundaries of the process, that is at $t = t_{stop}$ and $t = t_{stop} + \tau_{stop}$, respect to the value of the function in the limits $t \to \pm\infty$. On the other hand, in the case where `real_stop` = False, Re_o would fall linearly according to

$$Re_o(t) = -\frac{Re_o^{initial}}{\tau_{stop}} \cdot (t - t_{stop}) + Re_o^{initial} \tag{2.3}$$

The last control parameter to be specified in the input file concerns an other important feature of this subroutine: the time-step of the simulation during the stopping process is fixed to a constant value `dt_stop`. Although

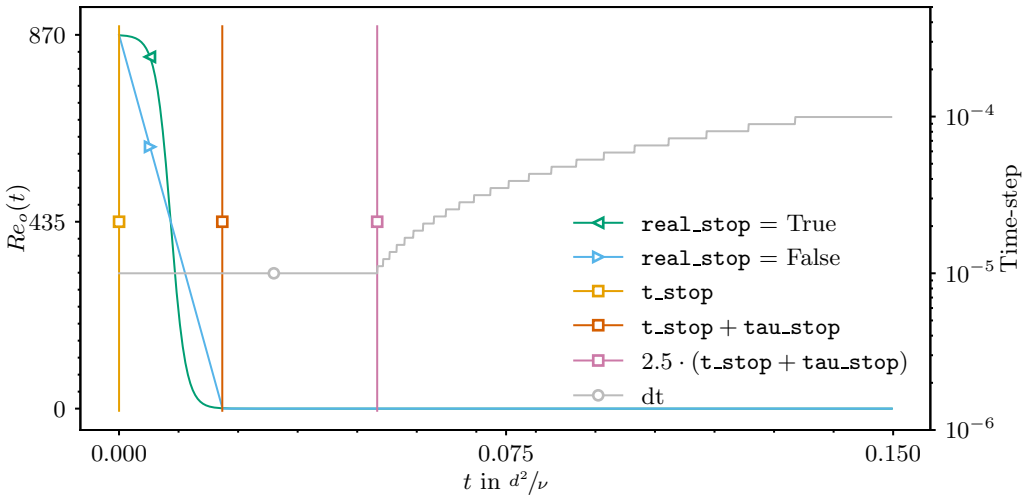

Figure 2.2: Subroutine `OuterReynolds` control on `nsCouette` simulation parameters.

`nsCouette` already is equipped with an adaptive time–step routine, it is also true that such feature is implemented bearing in mind that both Re are stable in time, meaning the problem is not a transitory one. The choice of fixing the times–step can be reasoned by the fact that the generation and early decay of the turbulence generated in our transitory problem by a rather quick stopping process is a really fast phenomena which needs a stable and pretty low simulation time–step. We think this is necessary if one wishes to obtain results corresponding to the actual physics observed during the experiment. Moreover, we decided to expand the time window where dt = `dt_stop` beyond the stopping process, so that the time-step is fixed in the time interval $[0.95 \cdot$`t_stop` ; $2.5 \cdot$(`t_stop`+`tau_stop`)], that is between 95% of the instant where the stopping process starts and 250% of the instant where it ends. We enlarged the window much more after the cylinder is stopped because it is then where the turbulent behaviour appears and therefore a finer temporal resolution shall be needed.

Another most important feature which has been newly implemented in the code concerns the initial perturbation in the flow. That is, in order to study how disturbances in the flow behave and temporally evolve in different situations, the flow must be "manually" disrupted by adding numerical perturbations that will decay or grow or change depending on the case. Otherwise, we could increase Re_o or Re_i or both as much as we wanted and we would see an invariant laminar flow in the system.

Hence, the new subroutine `pulse_init2` generates a random perturbation of amplitude $\sim 10^{-4}$, across the whole flow field, in all 3 directions, at the

beginning of the simulation as initial conditions.

2.3 Spatial and temporal resolution

The input file from `nsCouette` allows the user to select the number of grid points in each direction of the system as well as the time–step to be used during the simulation, hence the spatial and temporal resolution can be set at will. The question to be asked now is indeed, how can we fix such parameters?

Figure 2.3 represents an example for $Re_o = 3000$ of the conditions to be met as far as the spatial resolution is concerned in order to secure correct simulation results. Subplot **a** presents several E_θ and E_z energy modes temporal profiles during a simulation, in the $\hat{\theta}$ and $\hat{z}$ direction respectively. Such profiles allow us to see clearly there is an increase in the energy modes in both directions due to the stopping process. That is actually the generation and growth of turbulence which will be discussed later in the results section. Nonetheless, we can in fact locate where is placed the most critical point during the simulation, meaning where the flow perturbation is most intense and strongest. That is indeed when the energy of the modes is maximal. Therefore, we need to ensure that at such point the spatial resolution is sufficient.

We check that by looking at the energy spectrum in the $\hat{\theta}$ (subplot **b)**) and $\hat{z}$ (subplot **c)**) directions. In order to guarantee there are no errors when solving the Navier–Stokes equations, the *Energy Cascade* must be visible in the spectra, meaning that the largest structures, represented by the lowest k modes, in both directions must carry most of the energy in the system while the smallest, represented by the largest k modes, must hold little energy. Thus, there is no energy accumulated in the largest modes, which means that the viscous dissipation is well solved. The number of Fourier modes is directly linked to the number of points in the homogeneous directions.

In **b** and **c** we plotted several energy spectra for different critical instants of time during the simulation, corresponding mainly to the period where the perturbation is largest. We can see that in both subplots E_θ and E_z drop more than 4 orders of magnitude between the energy of the lowest mode (mode 0) and the energy of the largest mode. Such difference in large enough. Furthermore, there is no local maximum in the spectra for the largest modes that would indicate that there is an energy accumulation. All this information confirms that the spatial resolution fixed in this case for $Re_o = 3000$, which actually is `m_r` = 144, `m_th` = 96 and `m_z0` = 256 (see input file), is sufficient.

On the other hand, figure 2.4 represents an example for $Re_o = 1700$ of

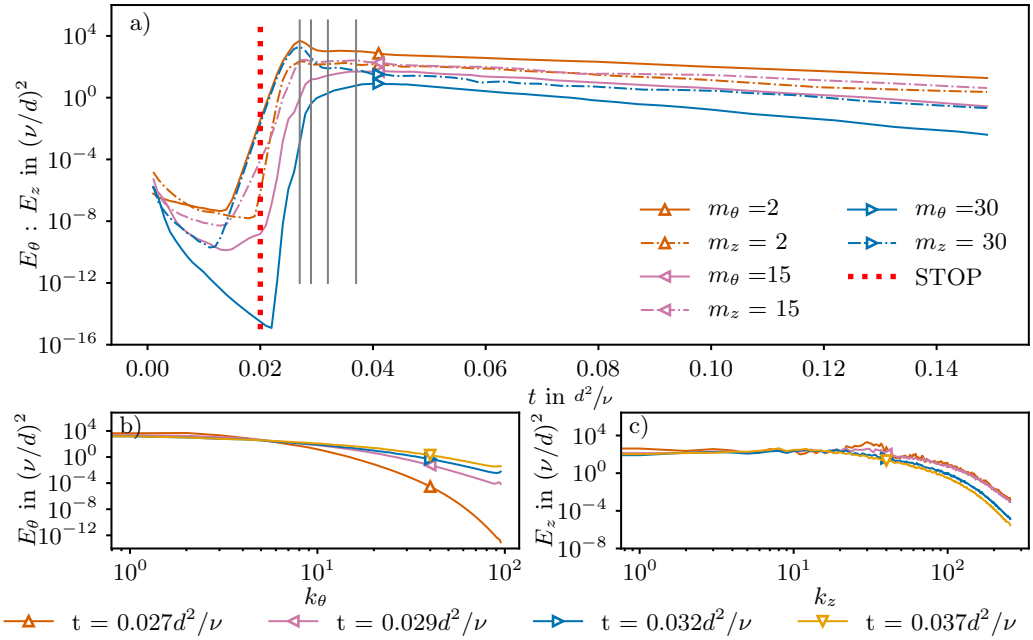

Figure 2.3: Spatial resolution criterion for numerical simulations. **a)** Azimuthal E_θ and axial E_z energy modes temporal profiles. $Re_o = 3000$. The grey vertical lines indicate the instants for which the energy spectrums have been represented in **b** and **c**. **b)** Azimuthal energy spectrum for different instants of time. **c)** Axial energy spectrum for different instants of time. We fixed `t_stop` = $0.00001d^2/\nu$, `tau_stop` = $0.02d^2/\nu$ and `real_stop=True`.

the procedure we used to select a suitable time–step for the stopping process `dt_stop`. In this case, an empirical approach was undertaken. A first simulation is run with an estimation of an adequate value for `dt_stop` and the energy modes temporal profiles are plotted. For instance, in **a)** the solid lines represent the profiles for some energy modes in the $\hat{\theta}$ direction with `dt_stop` $= 10^{-6}\ d^2/\nu$. If the results look reasonable (the physic is well reproduced), then we launch again the simulation with the same spatial grid but increasing `dt_stop`. We then plot again the temporal profiles for the same modes and compare them with the previous simulation. If both simulations output the same results, this means the larger `dt_stop` is already small enough in order to produce correct simulations, and therefore shall be chosen to run other simulations. For instance, the cross markers in **a** represent the profiles for the same modes but with `dt_stop` $= 10^{-5}\ d^2/\nu$. Furthermore, in **b** we have computed the absolute error $|\epsilon|$ between the profiles with `dt_stop` $= 10^{-5}\ d^2/\nu$, $E_\theta(dt = 10^{-5}d^2/\nu)$, and the profiles with `dt_stop` $= 10^{-6}\ d^2/\nu$, $E_\theta(dt = 10^{-6}d^2/\nu)$. We can see that it is of the order of 10^{-6} for most part of the simulation, meaning thereby that the outcome is the same whether `dt_stop` $= 10^{-5}\ d^2/\nu$ or `dt_stop` $= 10^{-}\ d^2/\nu$. We can then launch a simulation for `dt_stop` $= 10^{-4}\ d^2/\nu$ and check again the results and see if a larger time–step produces the same outcome. This procedure can be repeated as much as required until the convergence in the results is lost. The largest `dt_stop` which provides the same results compared to simulations with smaller `dt_stop` values should be regarded as the suitable value and shall be used to run other simulations.

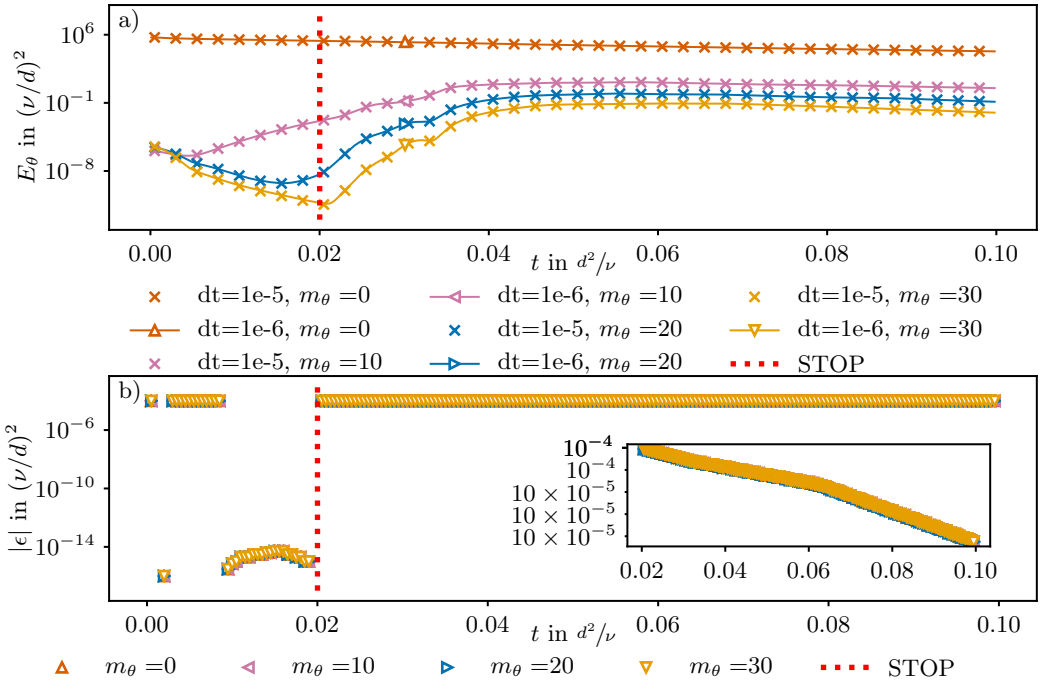

Figure 2.4: Temporal resolution criterion for numerical simulations. $Re_o = 1700$. **a)** Modal azimuthal energy E_θ modes temporal profiles for different time-steps, $dt = 10^{-5}d^2/\nu$ (x markers) and $dt = 10^{-6}d^2/\nu$ (solid lines). Time–step in viscous time units (d^2/ν). **b)** Absolute error $|\epsilon|$ between $E_\theta(dt = 10^{-5}d^2/\nu)$ and $E_\theta(dt = 10^{-6}d^2/\nu)$ for each mode respectively. Additional subplot has been added to zoom in the window $0.02 < t\nu/d^2 < 0.1$. We fixed `t_stop` $= 0.00001d^2/\nu$, `tau_stop` $= 0.0017d^2/\nu$ and `real_stop=True`.

3. Results

3.1 Qualitative comparison:

3.1.1 Onset of instability: vortical structures

Hence, `nsCouette` is now able to decrease the value of the outer cylinder Reynolds number from an initial value Re_o to 0 in a fixed amount of time `tau_stop`. It is specified in [5] that for the largest Re_o studied, the outer cylinder took approximately 0.0017 viscous time units to come to a halt. Therefore, in order to contrast the numerical outcome with the experimental results, we fixed in the input file `tau_stop` = 0.0017.

`nsCouette` is also build so that the simulation starts from a laminar regime. Since for the configuration considered (outer cylinder rotating and inner cylinder stationary), the flow is stable and thereby laminar, there is no need to waste simulation time waiting for the system to stabilise from the initial perturbation. Waiting simulation time before starting the process of stoppage would only affect the initial perturbation, which would decay and lose amplitude. Therefore, we fixed in the input file `t_stop` = 0.00001 without worrying.

Now, even if the code successfully drops Re_o to 0, that doesn't mean that the physics observed in the experiments will be reproduced. Hence, the first step will be to compare qualitatively the behaviour of the flow during the simulation with the results presented in [5], for instance figure 1.1. As explained in [5], in the experiment the fluid is mixed with a colorant and the $r - z$ cross-section is illuminated with a continuous laser while recorded by a camera. Thanks to the binarisation of the images, the experimentalists are able to observe the fluid's structures inside the flow. Nonetheless, in our numerical study we would not be able to produce such results by means of optical imagery and post-processing. Instead we do have access to the flow's velocity field, in any direction, over the entire gap width axially, at any azimuthal position and at any time. In the present study, the radial velocity (which is natural variable to describe vortical motion) is used to compare with the experimental visualizations.

Figure 3.1 represents both the scalar field $u_r(r, z)$ on the background, in logarithmic scale quantified by the colorbar, and the vector field $(u_r(r, z), u_z(r, z))$ on top of it using black arrows to point the direction and magnitude of the flow in each position. This figure associates the representation of $u_r(r, z)$ with the presence of vortical structures in the flow. Thanks to the additional field $u_z(r, z)$, we can clearly identify the vortexes by looking at the arrow streams (we can see rotating structures, clockwise and counter-

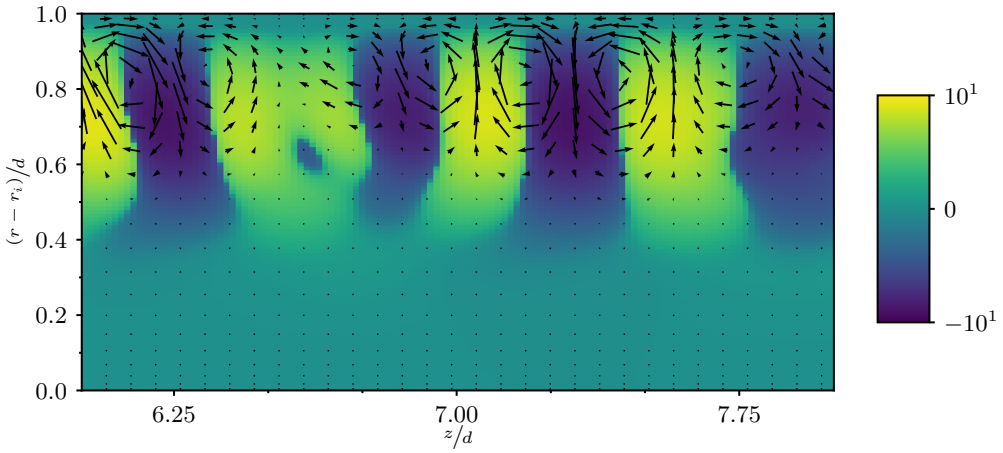

Figure 3.1: Axis-symmetrical vortexes near the outer cylinder for $Re_o = 1700$. On the background, the radial velocity scalar field $u_r(r, z)$ is represented on a logarithmic scale (colorbar) for a segment of the axial height. On top, the cross-section velocity vector field $(u_r(r, z), u_z(r, z))$ is represented using black arrows, showing thus the flow of the system. This cross–section corresponds to $t = 0.025d^2/\nu$. Note that the system has been rotated by 90 degrees counterclockwise.

clockwise consecutively). Furthermore, we can observe that for $u_r(r, z) < 0$ (color *blue*) the arrows point towards the inner cylinder, while for $u_r(r, z) > 0$ (color *yellowish green*) the arrows point towards the outer cylinder. Even though this might not be very significant, the important point is to notice that the separation of colors actually indicates where the center of the vortex is located. Observe that $u_r(r, z)$ presents a clear pattern of bands, chromatically sequential. Each vortex exists in half a blue band and half a yellowish band. The magnitude of $u_r(r, z)$ also indicates us in which radial region is the vortex present. We can see that for $0 < (r - r_i)/d < 0.5$ the arrows are negligible, therefore meaning there are no vortices, i.e. $u_r(r, z) \approx 0$ (bluish green color). Hence, the scalar field $u_r(r, z)$ actually reveals two pieces of information: the presence of vortical structures and their location in the cross–section.

Therefore, we build now figure 3.2 out of 2 different kinds of plot: on the top of the figure, several cross-sections of $u_r(r, z)$ are displayed at different instants of time, similarly to the experimental results presented in figure 1.1, respect to a unique logarithmic scale (colorbar on the right); on the bottom of the figure, the temporal evolution of $Re_o(t)$ is shown (in black) as well as the variations for different axial energy modes. The grey vertical lines correspond to the distinct instants of time for which the $u_r(r, z)$ field has been represented

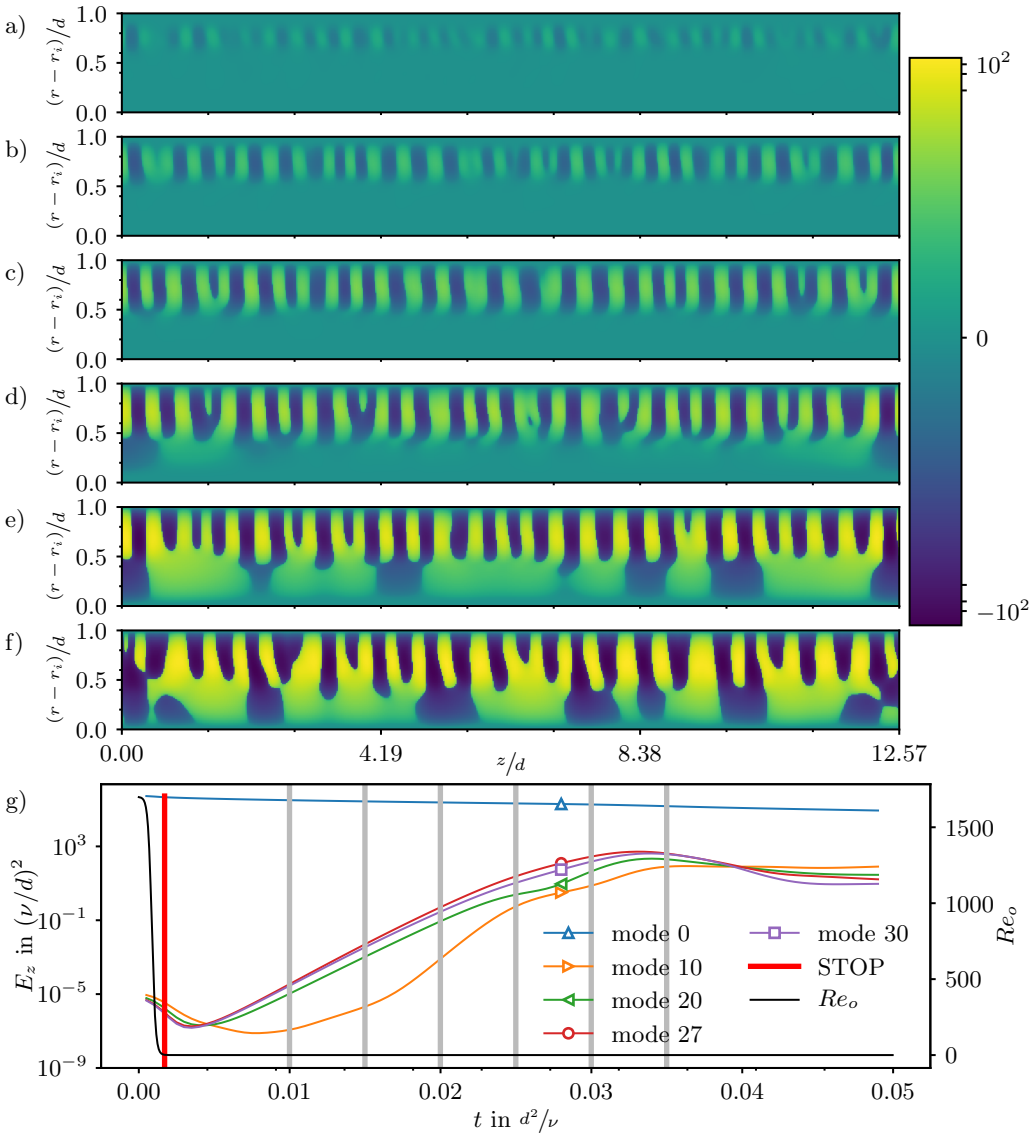

Figure 3.2: Generation and growth of turbulent eddies in an abruptly stopped numerical Taylor–Couette flow for $Re_o = 1700$. Subplots **a)** to **f)** represent the radial velocity field $u_r(r, \theta)$ over the whole axial height (z) at different instant in time in logarithmic scale, all sharing the same scale (colorbar on the right). The different instants are: **a)** $t = 0.01d^2/\nu$; **b)** $t = 0.015d^2/\nu$; **c)** $t = 0.02d^2/\nu$; **d)** $t = 0.025d^2/\nu$; **e)** $t = 0.03d^2/\nu$; **f)** $t = 0.035d^2/\nu$. Subplot **g)** represents the energy temporal evolution for different axial modes, as well as the Re_o profile. The grey vertical lines correspond to the different instants at which the $u_r(r, \theta)$ field has been represented.

on top. Thereby, figure 3.2 describes accurately how the flow changes during the simulation's first instants. We can observe how a band pattern appears near the outer cylinder, indicating the presence of small vortical structures, from approximately $t = 0.01d^2/\nu$, and then slowly grow towards the inner one while deforming and reorganising until filling the whole radial gap at approximately $t = 0.030d^2/\nu$. Before $t = 0.01d^2/\nu$ the magnitude of $u_r(r, z)$ is too low to observe the presence of vortices, and after $t = 0.030d^2/\nu$ the structures are already destabilised and chaotic. This can be clearly seen in subplot **g**, which yields a lot of information. In a first instance, we observe how the energy decreases and it is only after the outer cylinder is completely stopped that the axial modes start gaining energy. We are not talking of course of mode 0, which holds the average energy of the system (axially), and as there is no longer an input of energy because both cylinders are static, its profile progressively decays. Hence, while the outer cylinder rotates at constant speed the initial perturbation of the system decays, agreeing with the analytical prediction which states that the flow is stable in a TC system where only the outer cylinder rotates, independently of Re_o. Then, when the outer cylinder is abruptly stopped, the flow becomes unstable and the perturbation gains energy. We observe the presence of a dominant mode in **g**, which corresponds to axial mode 27, which indicates the presence of 27 pairs of vortices in the flow. That is exactly why we count 54 ($= 2 \cdot 27$) bands, in subplot **c** for instance. Knowing that a vortex exists in two halfs from two different bands, that means there is actually 54 vortexes, consistent with what we mentioned earlier. Then, when the simulation arrives to $t \approx 0.035d^2/\nu$ we see that both mode 27 and mode 30 are almost overlapped. Further in time, all modes represented (except mode 0) cross each other. This behaviour is what characterises the destabilization of the vortical structures. While during a vast period of the vortical growth there exists a dominant mode which dictates the number of vortices in the flow, at some point different modes become very similar in energy and there is a competition for the dominance. This competition destabilises the structures, continuously reorganising, and leads to increasingly more irregular structures. The numerical results from figure 3.2 agree with the experimental outcome obtained in [5] shown in figure 1.1.

The flow, now turbulent, will continue to grow and then start decaying, initiating then the second phase of the process described in [5].

3.1.2 Triphasic phenomena: Space-Time diagram

By taking the values of the scalar field $u_r(r, z)$ along the whole axial height at a fixed radial position in the gap at different instants in time during the

simulation, one can produce what is known as a Space–Time diagram (STD). Figure 3.3 presents the STDs obtained in simulations conducted at different values of Re_o near the outer cylinder, approximately at $(r - r_i)/d \approx 0.8$, as well as the experimental results exhibit in [5]. Subplot **a** represent the STD for $Re_o = 870$, where we only see a pattern of bands. As we explained in figure 3.1, this pattern is a clear indicator of the presence of vortical structures in the flow. Therefore, we observe that for such a low Reynolds number ($Re_o = 870$) the flow doesn't become turbulent, but instead the vortical structures grow and then progressively decay without destabilisation. This behaviour is consistent with the experimental results in [5] which state that no turbulence flow was observed for $Re_o < 870$.

Now, when we increased Re_o, the flow seems to change along the simulation. In fact, 3 phases can be identified in the STDs. Such phases have been pointed out in subplot **f**, which corresponds to a zoom of the STD represented in subplot **d** ($Re_o = 4400$). In a first instance we can observe the band pattern, corresponding to a regime with vortical structures. This is phase I. Shortly after, phase II starts as the band pattern is disrupted, meaning that the vortices are interacting and reorganising into different tumultuous structures. Such motif is a clear indicator of turbulent flow in a STD, and corresponds to the second phase of the process. Finally, the turbulent flow reorganises into bigger structures and regains a non-turbulent behavior, slowly decaying in magnitude. This corresponds to the last phase of the process, phase III, characterised by a purely viscous decay of the flow.

Subplot **g** corresponds actually to the experimental results presented in [5], the STP obtained for $Re_o = 1700$. Such plot is ideal to contrast the numerical results obtained with `nsCouette` and the experimental results from H. Singh and A. Prigent. We can clearly see that both subplots **b** and **g** (both for $Re_o = 1700$) are very similar, and that the flow behaviour is well reproduced numerically indeed, also for other values of Re_o.

Furthermore, we can also observe that the turbulent phase lasts longer for higher Re_o, statement reported as well in [5]. For instance, for $Re_o = 3000$ **c** the turbulent regime appears at $t \approx 0.02d^2/\nu$ and ends at $t \approx 0.1d^2/\nu$, which means a duration of $\Delta t \approx 0.08d^2/\nu$. On the other hand, for $Re_o = 6500$ **e** the turbulent regime appears at $t \approx 0.05d^2/\nu$ and ends at $t \approx 0.2d^2/\nu$, which means a duration of $\Delta t \approx 0.15d^2/\nu$. For phase III, we observe that the larger structures last longer as well as Re_o increases, which agrees with the experimental observations.

Figure 3.4 represents 3 different STD for the same $Re_o = 3000$ but at different radial positions in the gap, and unveils new results which couldn't be reported experimentally in [5]. We can observe that the band pattern, thus vortices, appear earlier in STD **c** which corresponds to $(r - r_i)/d \approx 0.8$,

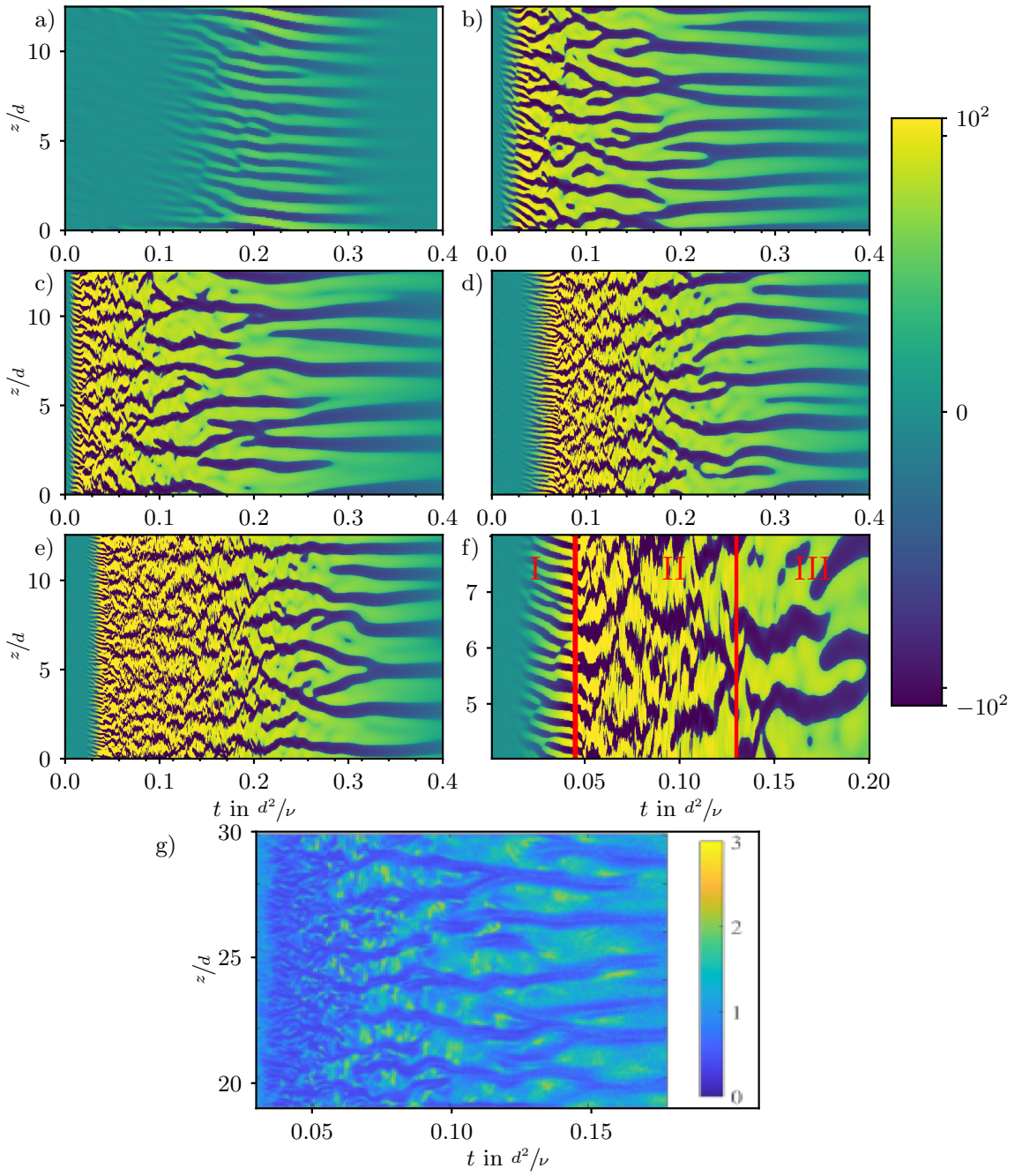

Figure 3.3: Space–Time diagram for increasing values of Re_o. The values of $u_r(r, z)$ have been taken along the whole axial height, at a fixed radial position corresponding to $(r - r_i)/d \approx 0.8$, at several instants of time. **a)** $Re_o = 870$; **b)** $Re_o = 1700$; **c)** $Re_o = 3000$; **d)** $Re_o = 4400$; **e)** $Re_o = 6500$; **f)** $Re_o = 4400$ (zoom). **g)** Experimental STP for $Re_o = 1700$.

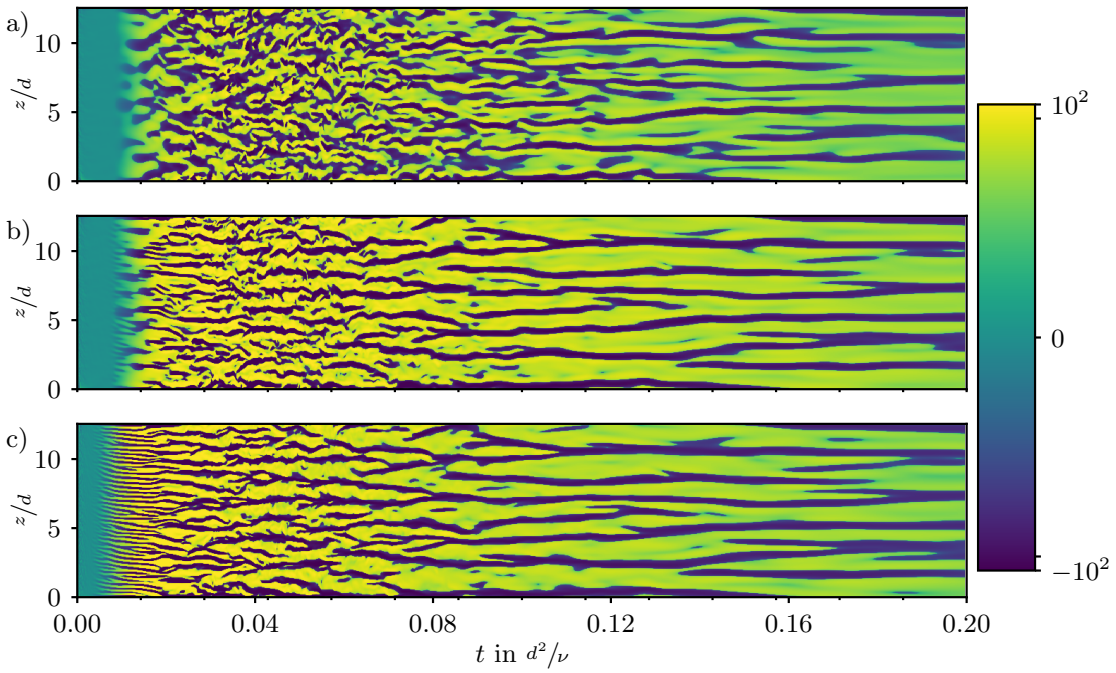

Figure 3.4: Space–Time diagram at different positions in the gap for $Re_o = 3000$. **a)** $(r - r_i)/d \approx 0.25$; **b)** $(r - r_i)/d \approx 0.5$; **c)** $(r - r_i)/d \approx 0.8$.

hence appear earlier near the outer cylinder. They grow then towards the inner cylinder, as we can see in STD **b** where a faint band pattern can be appreciated at the very beginning but still later than in **c**.

Moreover, it seems that the turbulence lasts longer near the inner cylinder, as we can see in STD **a**: while the turbulent phase ends at $t \approx 0.11d^2/\nu$ in **b** and at $t \approx 0.1d^2/\nu$ in **c**, the turbulent pattern in **a** ends at $t \approx 0.14d^2/\nu$, where we recover large and more regular structures. This turbulence looks also more chaotic near the inner cylinder, where we find smaller structures in the STD, both in time and in axial length. More of this structures are blue, which means $u_r < 0$. That is because the inner cylinder is receiving a lot of fluid from the gap's outer region due to the momentum generated by the vortices near the outer cylinder.

3.2 Quantitative comparison:

3.2.1 Vortex's growth

Following the study presented in [5], we are interested now in studying how the vortical structures observed during the numerical simulations are gener-

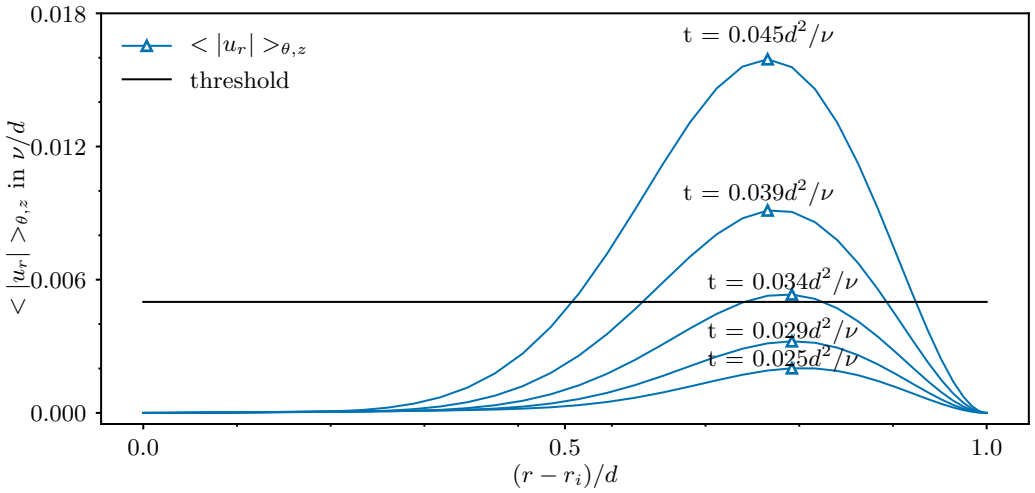

Figure 3.5: Vortex's width measurement methodology. Different $< |u_r| >_{\theta,z}$ radial profiles are plotted for different instants of time, for $Re_o = 870$. A threshold value is fixed so that the width of the vortex corresponds to distance between the intersections of the profile with the threshold.

ated and grow towards the inner cylinder. Once again, the study presented in [5] analyses this features using binarized images of the gap; once again, we will work with the radial velocity. Nonetheless, we will not use in this case the whole field $u_r(r, z)$, but instead we will be producing results using the absolute value radial velocity radial profile, averaged over the homogeneous directions θ and z, that is $< |u_r| >_{\theta,z}$. The absolute value is necessary, otherwise the profile would be almost 0 during the phase where the vortical structures are generated and grow. That is because, as we have seen already in figure 3.2, during the presence of vortices u_r appears as a pattern of band along the z axis, with sequentially positive values followed by negative ones, and *vice-versa*. Then, if we would attempt computing an average over z of u_r we would most certainly obtain a negligible profile, which would be useless. On the other hand, if one averages axially $|u_r|$ instead of u_r, the profile resulting will reflect the radial dependence of the intensity of the field. Now, by looking again at figure 3.1 we can see that in fact the arrows have a longer radial (vertical in the figure) component approximately at the same radial position as the center of the vortexes themselves. This ultimately means that the radial profile $< |u_r| >_z$ maximum should yield the average radial position of the center of the vortical structures in the gap. The same goes for $< |u_r| >_{\theta,z}$ of course. Hence, $< |u_r| >_{\theta,z}$ is indeed a very useful tool to analyse and study in average the behavior of vortices in the flow.

Figure 3.5 presents several radial profiles of $< |u_r| >_{\theta,z}$ for different in-

stants of time. We observe that the profiles grow with time and that the maximum of the profile (indicated with the marker) moves towards the inner cylinder, which is consistent with the movement of the vortices observed. Furthermore, a black line is plotted and represents the threshold of measure. That is because we plan to measure the average radial width of the vortical structures using this profile $< |u_r| >_{\theta,z}$. Indeed, if the radial position of the maximum would approximately represent the average radial position of the vortices center, then by the same argument one can think that the profile is actually reflecting the whole average radial structure of the vortices, again looking at figure 3.1 to support the explanation. The average radial width would then be the radial interval for which the profile is different from 0. However, similarly to experimental instruments of measure, we fixed a lower threshold value and will consider no existence of a vortical structure if the profile is underneath such threshold. Hence, the average radial width of the vortices $\delta_r(< u_r >_{\theta,z})$ is computed, graphically, as the radial distance between the intersections of $< |u_r| >_{\theta,z}$ and the threshold line, or analytically as the distance

$$\delta_r(< u_r >_{\theta,z}) = \left| r_2 - r_1 \right| \qquad \text{with} \qquad r_{1,2} = r\Big|_{<|u_r|>_{\theta,z}(r)=threshold}$$

Using this methodology, we obtain the results presented in figure 3.6. In subplot **a** are represented $\delta_r(< u_r >_{\theta,z})$ of the vortices during the simulation for different Re_o. We can observe that except for $Re_o = 870$, in all other simulations the vortices rapidly fill the whole gap between cylinders. Furthermore, we notice that as Re_o increases, the growth starts earlier, meaning that the vortices in fact appear earlier in the flow for higher values of Re_o. Nonetheless, such temporal delays are clearly very short, of the order of 10^{-2} viscous time units.

On the other hand, in subplot **b** is represented the same data from subplot **a**, but only the growing phase of the vortices is considered in this case. That is, we just represented the values of $\delta_r(< u_r >_{\theta,z})$ which are not 0 (the vortices didn't appear yet) nor 1 (the vortices have filled the gap), for different values of Re_o. We can distinguish different phases of growth for $Re_o > 870$. This can clearly be seen in subplot **b**. There exists a saturation phase at the end of the growth, approximately when the vortices fill the inner half gap between the cylinders, that is for $0.5 < \delta_r(< u_r >_{\theta,z}) < 1$. Nonetheless, we also observe a first phase of growth which seems to follow a power law scaling, that is $\delta_r(< u_r >_{\theta,z}) \sim t^{\xi}$. As such, we though it was pertinent to use a logarithmic scale to present the data. As mentioned in [5], the experimental results show that such growth phase can be well fitted using a power law with exponent 1/2, meaning that the vortices grow as $\sim \sqrt{t}$. Such tendency

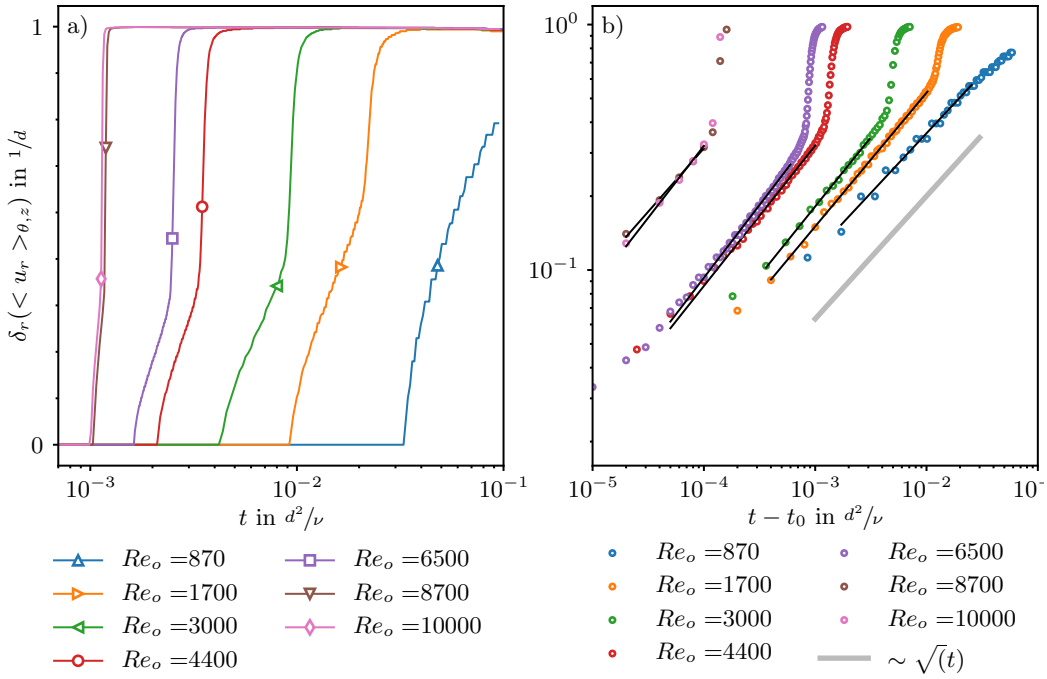

Figure 3.6: Growth of vortices in the gap for different Re_o. **a)** Radial width of the vortices (linear scale) in real simulation time (logarithmic scale). **b)** Radial width of the vortices (logarithmic scale) during the period of growth. t_0 corresponds to the instant where the vortices appear and start growing.

Re_o	870	1700	3000	4400	6500	8700	10000
Coefficient	0.4862	0.5446	0.5636	0.5721	0.5931	0.5162	0.5853

Table 3.1: Vortex's growth power-law fitting coefficients for different Re_o. The width of the vortex is computed using the radial profile $< u_r >_{\theta,z}$.

has been plotted in grey in subplot **b** in order to compare graphically. As we can see, during the first growth phase all Re_o seem to adjust properly to such fitting. Going further, we calculated the power law exponents ξ fitting the growth phase for the different Re_o by solving the least square problem; such fittings are represented in subplot **b** as black lines. The corresponding exponents are given in table 3.1. We can see that even though they are not exactly equal to 1/2, the exponents for all Re_o are pretty close to such a value, inside the interval [0.4862 ; 0.5931]. The fluctuations around 0.5 may be attributed to the methodology described earlier, as well as the threshold value.

As stated in [5], this numerical results are also in very good agreement

with the results obtained by Kaiser *et al* (2020) [6]. However, the magnitude measured by Kaiser *et al* (2020) was not the vortex's radial width, but instead they measured the radial width of the unstable zone in the flow and found that it grows as $\sim \sqrt{t}$. H. Singh and A. Prigent (2021) argue in [5] that $\delta_r(< |u_r| >_{\theta,z})$ may be regarded as the the width of the unstable zone in the flow appealing the fact that the vortexes are originated in such region as interpenetrating spirals do in the unstable zone between the inner cylinder and the nodal surface (the cylindrical surface where $u_\theta = 0$) in counter-rotating TC flow. We might as well look deeper into the origin of the vortical structures in the flow.

3.2.2 Origin of instability

It is clear by observing the temporal evolution of the flow that, for all values $Re_o \geq 870$, vortical structures appear near the outer cylinder shortly after it is abruptly stopped. However, we are now interested in investigating by which mechanism, or mechanisms, these vortices are generated. Both H. Singh and A. Prigent (2021) [5] and Kaiser *et al* (2020) [6] state that the origin of the vortices points towards a centrifugal instability in the flow. This kind of instability, often known in rotating fluid systems, is characterised by the fact that the interior layers of fluid are moving faster that the exterior layers, which creates an angular momentum gradient (in the radial direction). The interior fluid then centrifuges its way towards the exterior walls, generating vortical structures in the flow. All the process is driven by inertial, which is why sometimes it is also called inertial instability. Although the occurrence of this instability type was speculated by the experimentalists, it could not be verified using the experimental data. We show with our numerical data that this is indeed the case.

Figure 3.7 represents several radial profiles of the azimuthal velocity component, averaged azimuthally and axially, that is $< u_\theta >_{\theta,z}$, for different instants of time, with $Re_o = 4400$. We observe that while the outer cylinder is steadily rotating, the analytical profile of the Taylor–Couette flow is recovered in the simulation. However, as soon as the outer cylinder is stopped, $< u_\theta >_{\theta,z}$ drops to 0 at the outer wall, consistent with the no-slip boundary conditions imposed. Meanwhile, the velocity in the gap remains non-zero, fulfilling then the conditions for a centrifugal instability to appear. The centrifugal unstable zone will correspond of course to the region in the gap between $max(< u_\theta >_{\theta,z})$ and the outer wall, as in such region $< u_\theta >_{\theta,z}$ is lower in value than $< u_\theta >_{\theta,z}$ for lower values of r (hence the fluid in this region is rotating slower than in the inner layers). Moreover, we can see in figure 3.7 that $max(< u_\theta >_{\theta,z})$ is located near the outer wall and then

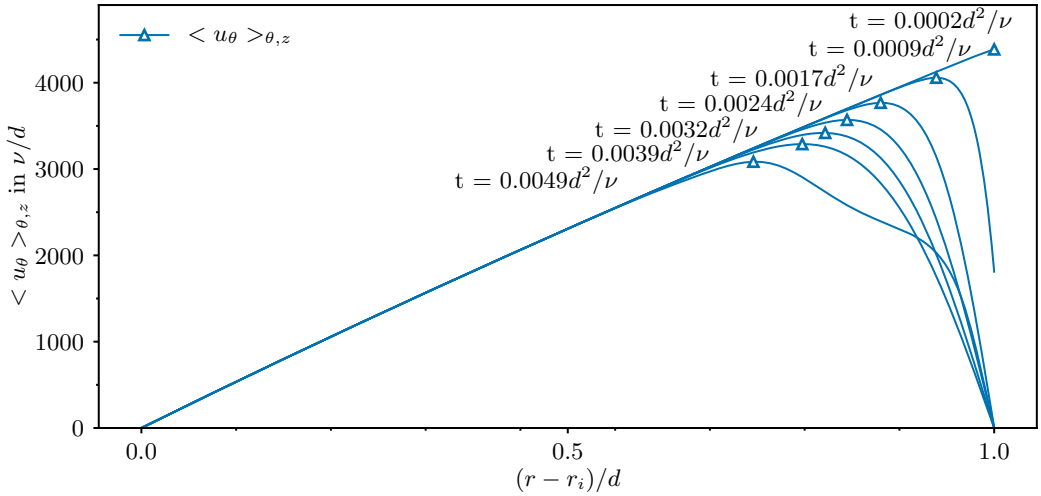

Figure 3.7: Decay of the $< u_\theta >_{\theta,z} (r)$ radial profile for $Re_o = 4400$. The markers on the profiles indicates the location of the maximum. The instant of time corresponding to each profile has also been specified following the same height sequence as the markers during the decay.

migrates rapidly towards the inner cylinder when the outer one is stopped. This means in fact that the centrifugal unstable zone grows rapidly at the beginning of the process, allowing then vortices to generate inside the region and grow as well, which agrees with the observations from [6].

One can also relay on the Rayleigh discriminant ϕ in order to measure the radial width of the unstable zone, such that

$$\phi(r) = \frac{1}{r^3}\frac{d}{dr}\big(L\big)^2 = \frac{1}{r^3}\frac{d}{dr}\big(ru\big)^2 = \frac{1}{r^3}\frac{d}{dr}\big(r^2 u_\theta\big)^2 \tag{3.1}$$

where L is the angular momentum, r is the radius and u is the total velocity (in a plane at height z_0). We adapted it to

$$\phi(r) = \frac{1}{r^3}\frac{d}{dr}\big(r^2 < u_\theta >_{\theta,z}\big)^2 \tag{3.2}$$

The Rayleigh discriminant ϕ is positive for stable regions and negative for unstable regions of the gap. Therefore, knowing that a centrifugal unstable region will develop near the outer wall shortly after it is stopped, and that at the same time the inner region is definitely stable, the ϕ profile should present a root at some radial position in the gap. In fact, the distance between the position of such root and the outer wall will allow us to measure the width of the centrifugal unstable zone.

Figure 3.8 shows qualitatively all these features. On each cross–section have been represented the radial profiles for $\phi(r)$, $< |u_r| >_{\theta,z}$ and $< u_\theta >_{\theta,z}$

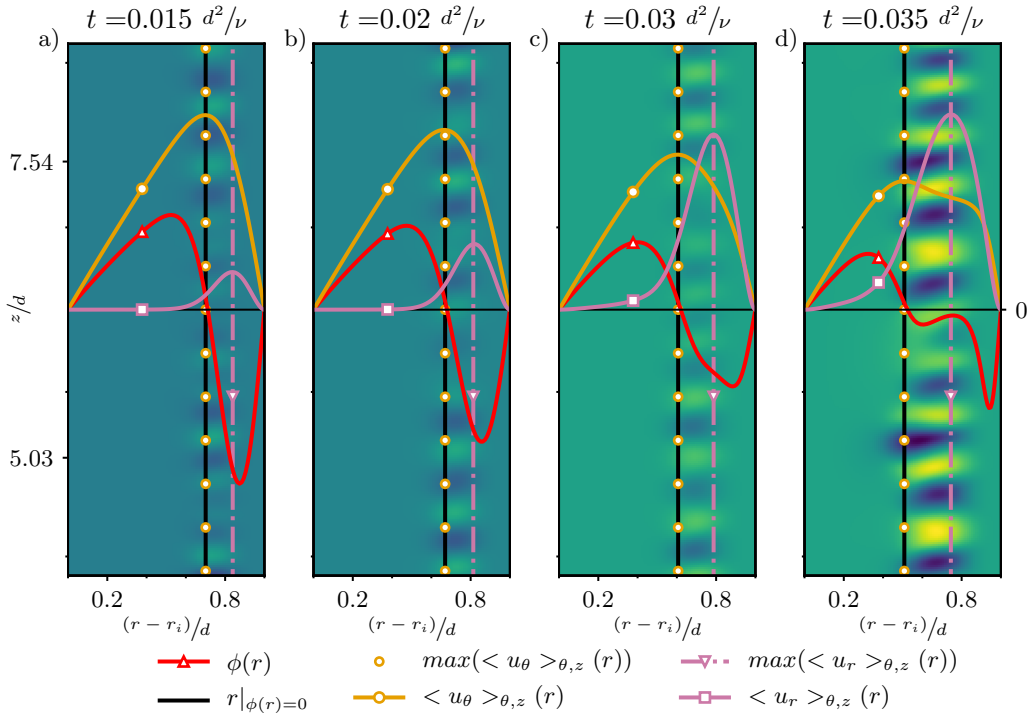

Figure 3.8: Centrifugal instability zone for $Re_o = 1700$. Several cross–sections of the TC system have been represented at different instants in time: **a)** $t = 0.015d^2/\nu$; **b)** $t = 0.02d^2/\nu$; **c)** $t = 0.03d^2/\nu$; **d)** $t = 0.035d^2/\nu$. In the background, the scalar field $u_r(r, z)$ is represented. On top, the radial profiles for $\phi(r)$, $< |u_r| >_{\theta,z}$ and $< u_\theta >_{\theta,z}$. The root of $\phi(r)$ is indicated by a vertical line, and so are the maximums of $< |u_r| >_{\theta,z}$ and $< u_\theta >_{\theta,z}$ respectively.

on top of the scalar field $u_r(r, z)$. The different vertical lines point out the radial positions for the root of $\phi(r)$ as well as the maximums of $< |u_r| >_{\theta,z}$ and $< u_\theta >_{\theta,z}$.

At first glance, we observe that, as expected, the Rayleigh profile ϕ is positive, thus stable, in the inner region of the gap while the area nearer the outer cylinder is negative, thus unstable. The location in the gap for the profile's root is indicated with a vertical black line, and we observe that such line migrates towards the inner cylinder as the simulation advances in time. Hence, as far as Rayleigh criterion is concerned, we can state that the centrifugally unstable zone appears near the outer cylinder and then grows towards the inner one.

Furthermore, we notice two important characteristics for the location of the $< u_\theta >_{\theta,z}$ profile's maximum (represented with orange circles): on one

hand, as we said before, the maximum move towards the inner cylinder; on the other hand, we can clearly see that such maximum is located at the same position as the ϕ's root. Therefore, both methods to measure the radial width of the centrifugal instability zone seem to be equivalent. Even though such observation might be just a coincidence existing at the instants of time represented, full temporal profiles for different values of Re_o confirm that both $max(< u_\theta >_{\theta,z})$ and $\phi(r)$'s root share the same radial location in the gap during the whole unstable region growth period.

Finally, we chose to plot the $< |u_r| >_{\theta,z}$ profile as well in order to pinpoint the radial position for the average center of the vortexes in the flow, corresponding to the location of the profile's maximum. Hence, based on this assumption, we observe in fact that for every instant of time the vortical structures' center is located inside the unstable region. We can therefore assume that the vortices are indeed generated inside the centrifugal instability zone. H. Singh and A. Prigent also comment in [5] that the size of the vortexes $\delta_r(< |u_r| >_{\theta,z})$ could be approximately considered as the width of the unstable zone of the flow. This means thereby that the unstable zone should also be growing as $\sim \sqrt{t}$. We have used our numerical data to verify such predictions.

Figure 3.9 presents the radial width of the unstable zone $\delta_r(< u_\theta >_{\theta,z})$ measured as the distance between the outer wall and the radial location of $max(< u_\theta >_{\theta,z})$, based on figure 3.7. In subplot **a** are represented the temporal profiles of $\delta_r(< u_\theta >_{\theta,z})$ for different values of Re_o in real simulation time. We can identify different stages of the growth. In a first instance, the unstable region grows steadily with a constant rate until it reaches a point where $\delta_r(< u_\theta >_{\theta,z})$ increases drastically. Such behaviour is similar to the one observed for $\delta_r(< |u_r| >_{\theta,z})$ in figure 3.6 **a**. A first local maximum is attained, after which the profile starts fluctuating. We consider that after such event the flow is already entering a stage of transition towards turbulence, and therefore is not part of the growth's process. Hence, we locate the period of expansion as the data between $\delta_r(< u_\theta >_{\theta,z}) = 0$ and its first local maximum. Such values are represented in subplot **b**, for each Re_o. Furthermore, we fitted the growths according to a power law function $\sim t^\xi$ with a suitable exponent and also plotted a $\sim \sqrt{t}$ grey slope in order to compare graphically.

The power law fittings exponents for $\delta_r(< u_\theta >_{\theta,z})$ growth are shown in table 3.2. We notice in fact that for $Re_o < 6500$, the values differ significantly from 0.5, and are also pretty different from the exponents obtained in table 3.1. Therefore, this means that the vortical structures growth doesn't match the growth of the centrifugal unstable region, but instead the unstable region seems to grow slower than the vortices because the exponents in table 3.1 are larger than the ones we obtained in table 3.2, at least for $Re_o < 6500$. Such

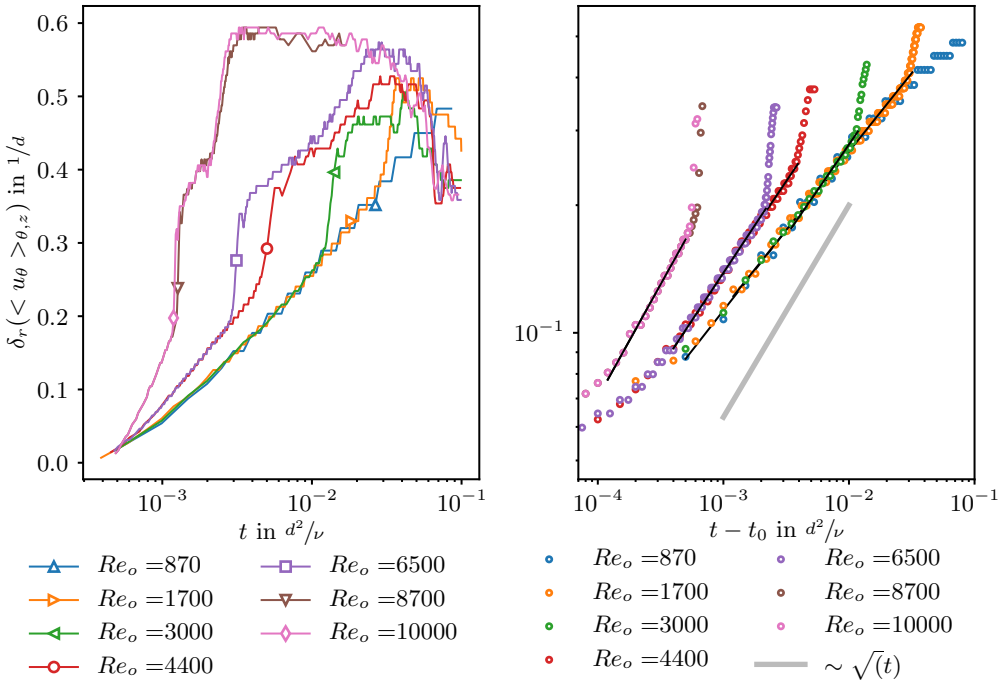

Figure 3.9: Centrifugal instability zone's growth. The width of the unstable region $\delta_r(< u_\theta >_{\theta,z})$ has been measured as the distance between the outer wall and the radial location of $max(< u_\theta >_{\theta,z})$. In **a)**, several temporal profiles of $\delta_r(< u_\theta >_{\theta,z})$ are plotted for different values of Re_o. In **b)**, only the growth period has been represented and fitted using power laws functions.

results don't agree with the statements presented in [5]. We believed the data post-processing may have been erroneous, however table 3.3 shows the computed unstable zone growth exponents obtained with simulations where `tau_stop` was fixed to 0.02 viscous time units. The same post-processing routine was used in order to produce such results. In this case, the exponents are very close to the 0.5 value expected. Even though such results are out of this study framework, we believe the stopping time `tau_stop` to be an important parameter yielding significant weight in this process, numerically or experimentally. Extending or reducing the stoppage time may affect the initial perturbation state when the centrifugal instability zone is generated near the outer cylinder. Future research may procure more insight on the effects of the parameter `tau_stop` during the stoppage of a TC system.

Re_o	870	1700	3000	4400	6500	8700	10000
$< u_\theta >_{\theta,z} (r)$	0.3782	0.3703	0.4302	0.4385	0.4478	0.5335	0.5335

Table 3.2: Centrifugal instability zone's growth power-law fitting exponents for `tau_stop` = 0.0017.

Re_o	870	1700	3000	4400
$< u_\theta >_{\theta,z} (r)$	0.5079	0.5074	0.5298	0.5304

Table 3.3: Centrifugal instability zone's growth power-law fitting exponents for `tau_stop` = 0.02.

3.3 Characterization of the free decay of inhomogeneous and anisotropic turbulence

3.3.1 Kinetic energy

The kinetic energy k of the TC flow during the simulation also provided some insight on the phenomena. Following the course of action presented in [5], we computed three different variants of k: the mean kinetic energy k_{mean}; the turbulent kinetic energy k_{turb}; and finally wind kinetic energy k_{wind}. The expressions for such magnitudes are respectively

$$k_{mean} = \frac{1}{2}\left[(< u_r >_{\theta,z})^2 + (< u_\theta >_{\theta,z})^2 + (< u_z >_{\theta,z})^2\right] \tag{3.3}$$

$$k_{turb} = \frac{1}{2}\left[< (u'_r)^2 >_{\theta,z} + < (u'_\theta)^2 >_{\theta,z} + < (u'_z)^2 >_{\theta,z}\right] \tag{3.4}$$

$$k_{wind} = \frac{1}{2}\left[< (u'_r)^2 >_{\theta,z} + < (u'_z)^2 >_{\theta,z}\right] \tag{3.5}$$

where $u'_{r,\theta,z} = u_{r,\theta,z} - < u_{r,\theta,z} >_{\theta,z}$ is the turbulent component of the velocity field for each direction respectively. The data is averaged in both homogeneous directions $\hat{\theta}$ and $\hat{z}$.

Figure 3.10 represents the different kinetic energy components temporal profiles for different radial positions in the gap, whereas at ${}^{(r-r_i)}/_d \approx 0.1,\ 0.25,\ 0.5,\ 0.75,\ 0.9$, for $Re_o = 4400$. Subplot **a** presents k_{mean} while subplots **b** and **c** are for k_{turb} and k_{wind} respectively. Finally, in subplot **d** we represented all the k for ${}^{(r-r_i)}/_d \approx 0.75$.

We first turn our attention towards k_{turb}. We can see that for all radial positions shortly after the outer cylinder is abruptly stopped, k_{turb} changes

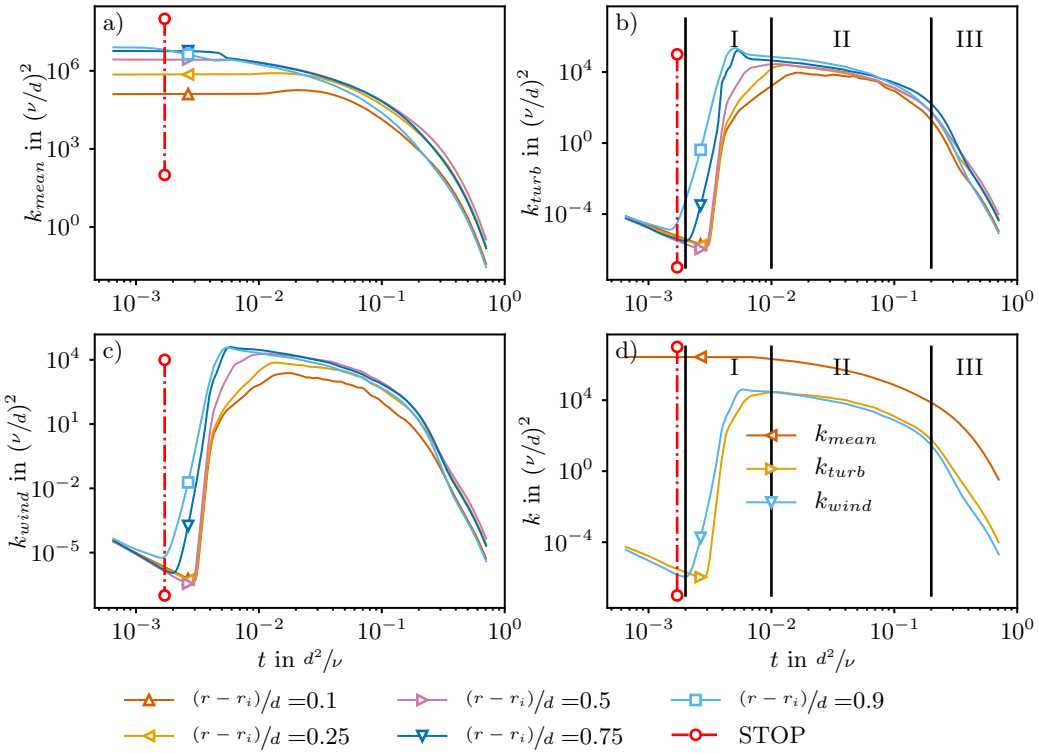

Figure 3.10: Kinetic energy variants temporal profiles at different locations in the gap, for $Re_o = 4400$. **a)** Profiles for k_{mean}; **b)** Profiles for k_{turb}; **c)** Profiles for k_{wind}; **d)** Profiles for the three variants at $^{(r-r_i)}/_d \approx 0.75$

from a decaying regime into a strongly generating one, during which almost 8 orders of magnitude are gained. In fact this phase corresponds to the phase where the vortices are generated, grow and then transient into turbulence, phase I described earlier. We can clearly see that both components k_{turb} and k_{wind}, computed from the turbulent fluctuations of the flow $u'_{r,\theta,z}$, increase during this phase, meaning that turbulence is appearing and growing. We also notice that the k_{turb} maximum, and the same for k_{wind}, is larger at $^{(r-r_i)}/_d \approx 0.9$ than at other locations in the gap. The growing also starts earlier for that profile. Hence, this results support the idea that the turbulence is generated earlier near the outer cylinder and that it becomes stronger there than in the rest of the gap. Afterwards, the decay of turbulence starts, which corresponds to phase II. We observe that all k_{turb} profiles, previously separated in magnitude, join together at this point, which means actually that the turbulence has spread from the outer cylinder towards the inner one, filling the whole gap. All profiles now decay slowly until reaching a transient region between phases II and III. We can clearly see that the slope

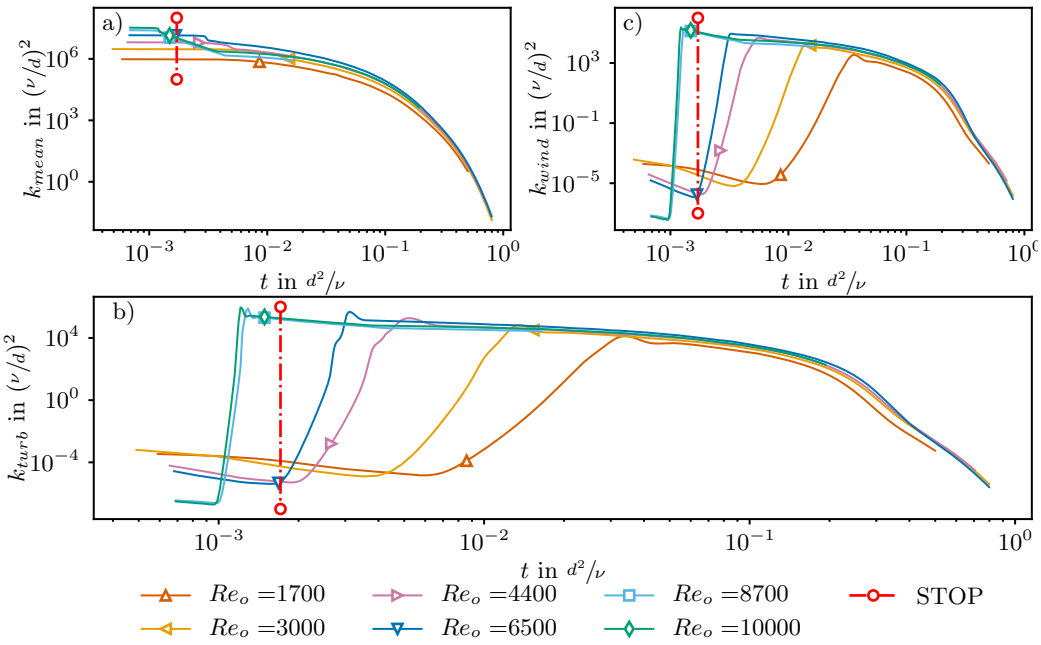

Figure 3.11: Kinetic energy temporal profiles for different value of Re_o, at $(r - r_i)/d \approx 0.8$. **a)** Profiles for k_{mean}; **b)** Profiles for k_{turb}; **c)** Profiles for k_{wind}.

in the decay changes, which physically reflects a change in the regime of the system, from a turbulent free decay (phase II) towards a viscous one (phase III).

Finally, we can take a look at k_{mean}, which simply decays from the moment the outer cylinder is stopped. The decay profiles are very similar for the different $(r - r_i)/d$, and the fact that at the beginning k_{mean} is larger near the outer cylinder is because that cylinder is the only one rotating, while the inner is static and then provides no energy to the system. These results agree with the experimental ones presented in [5].

Hence, we have now compared the different k variants respect to their position in the gap for the same Re_o. What can we say then if we compare them respect to different values of Re_o at the same radial location? Figure 3.11 presents several temporal profiles of the different k for various Re_o, at $(r - r_i)/d \approx 0.8$ fixed. We observe not much difference between simulations as far as k_{mean} is concerned (subplot **a**). However, both k_{wind} and k_{turb} reflect much more dissimilarities. We see that as Re_o increases, phase I appears earlier and lasts less time because the slope of the profile becomes steeper, which means turbulence is generated faster. Furthermore, it is very interesting to observe that all profiles are almost collapsing during the last stage of phase II, the transition from II to III and finally during the viscous

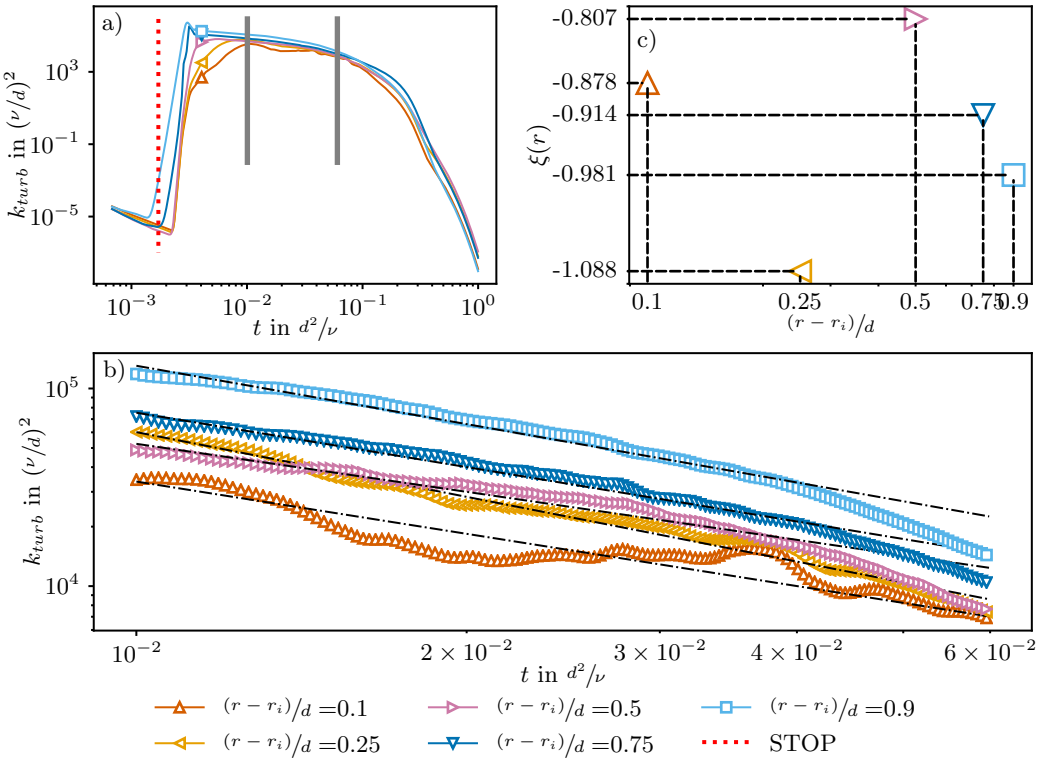

Figure 3.12: Turbulent kinetic energy k_{turb} decay exponents for $Re_o = 6500$. **a)** Turbulent kinetic energy temporal profiles for different radial positions in the gap. **b)** Turbulent kinetic energy temporal profiles and power-law fitting for the window marked in **a)** with grey vertical lines. **c)** Power-law fitting exponents for different radial positions.

decay in phase III. Therefore, it seems that such stages, both in magnitude and time (starting and duration), are independent of Re_o. Further research could reveal such behaviour dependents on other parameters of the process, maybe `tau_stop`. On the other hand, if all profiles transition to phase III at the same time but phase II starts earlier as Re_o increases, that means that phase II must be longer for higher Re_o, as we can clearly see in **b** and **c**. We already noticed such behaviour when looking at the STDs in figure 3.3. Quantitative data now confirms it.

Now, as we stated in the introduction, we are very much interested in characterising the free decay of turbulence in inhomogeneous and anisotropic flow. We recall that the $k-\varepsilon$ turbulence model requires information for both the turbulent kinetic energy k_{turb} and the turbulent energy dissipation rate ε_{turb}.

Hence, figure 3.12 presents the methodology we used to characterise k_{turb}'s

Re_o \ $(r-r_i)/\nu$	0.1	0.25	0.5	0.75	0.9
1700	-3.653	-3.108	-3.029	-2.463	-3.587
3000	-1.591	-1.837	-1.776	-1.488	-2.11
4400	-0.525	-1.077	-0.958	-1.04	-1.182
6500	-0.878	-1.088	-0.807	-0.914	-0.981

Table 3.4: Turbulent kinetic energy k_{turb} power–law fitting exponents during the turbulent decay.

free decay, for instance with $Re_o = 6500$. Subplot **a** represents the different temporal profiles for k_{turb} at several radial locations in the gap, similarly to figure 3.11 **b**. However, in this case we selected a temporal window marked with vertical grey lines for which we represented the data in subplot **b**. We point out that such window is located in phase II of the process, corresponding to the turbulent free decay of the flow. Now, in order to characterise the decay we fitted such data according to a power law model $\sim t^{\xi}$ and extracted the corresponding exponents in subplot **c**, plotted in logarithmic scale. Thereby, by proceeding as shown in this figure, we obtained the decay exponents ξ for the different values of Re_o, for different positions $(r-r_i)/\nu$ in the gap. We call attention to the fact that this characterisation of the decay is merely a fitting of the data obtained and would never presume to be regarded as a law of physics. Hence, the different exponents are presented in table 3.4. We notice that as we move towards the outer cylinder, a clear tendency in the exponents values may be observed, whereas ξ decreases as Re_o increases. Therefore, for higher Re_o the turbulent decay becomes slower near the outer cylinder. This makes sens according to the profiles in figure 3.11: if phase II lasts longer for higher Re_o while the transition to III is at the same time for all Re_o, phase II has to decay slower as Re_o increases.

3.3.2 Energy dissipation rate

Now that k_{turb} is characterised, we move towards the turbulent energy dissipation rate ε_{turb}, also necessary for the $k-\varepsilon$ model.

Proceeding similarly to [5], we computed the different energy dissipation rate components, whereas ε_{total}, ε_{mean} and ε_{turb}. Their expressions correspond to equations 3.6, 3.7 and 3.8 respectively.

$$\varepsilon_{total} = \nu \Bigg[2 \left(\left(\frac{\partial u_r}{\partial r} \right)^2 + \left(\frac{1}{r} \frac{\partial u_\theta}{\partial \theta} + \frac{u_z}{r} \right)^2 + \left(\frac{\partial u_z}{\partial z} \right)^2 \right) + \left(r \frac{\partial (u_\theta / r)}{\partial r} \right)^2 + \left(\frac{1}{r} \frac{\partial u_r}{\partial \theta} \right)^2 + \left(\frac{1}{r} \frac{\partial u_z}{\partial \theta} \right)^2 + \left(\frac{\partial u_z}{\partial r} \right)^2 + \left(\frac{\partial u_r}{\partial z} \right)^2 + \left(\frac{\partial u_\theta}{\partial z} \right)^2 + 2 \left(\frac{\partial (u_\theta / r)}{\partial r} \cdot \frac{\partial u_r}{\partial \theta} + \frac{1}{r} \frac{\partial u_\theta}{\partial z} \cdot \frac{\partial u_z}{\partial \theta} + \frac{\partial u_r}{\partial z} \cdot \frac{\partial u_z}{\partial r} \right) \Bigg] \tag{3.6}$$

$$\varepsilon_{mean} = \nu \Bigg[2 \left(\left(\frac{\partial \bar{u}_r}{\partial r} \right)^2 + \left(\frac{1}{r} \frac{\partial \bar{u}_\theta}{\partial \theta} + \frac{\bar{u}_z}{r} \right)^2 + \left(\frac{\partial \bar{u}_z}{\partial z} \right)^2 \right) + \left(r \frac{\partial \overline{(u_\theta / r)}}{\partial r} \right)^2 + \left(\frac{1}{r} \frac{\partial \bar{u}_r}{\partial \theta} \right)^2 + \left(\frac{1}{r} \frac{\partial \bar{u}_z}{\partial \theta} \right)^2 + \left(\frac{\partial \bar{u}_z}{\partial r} \right)^2 + \left(\frac{\partial \bar{u}_r}{\partial z} \right)^2 + \left(\frac{\partial \bar{u}_\theta}{\partial z} \right)^2 + 2 \left(\frac{\partial \overline{(u_\theta / r)}}{\partial r} \cdot \frac{\partial \bar{u}_r}{\partial \theta} + \frac{1}{r} \frac{\partial \bar{u}_\theta}{\partial z} \cdot \frac{\partial \bar{u}_z}{\partial \theta} + \frac{\partial \bar{u}_r}{\partial z} \cdot \frac{\partial \bar{u}_z}{\partial r} \right) \Bigg] \tag{3.7}$$

$$\varepsilon_{turb} = \nu \Bigg[2 \left(\left(\frac{\partial u'_r}{\partial r} \right)^2 + \left(\frac{1}{r} \frac{\partial u'_\theta}{\partial \theta} + \frac{u'_z}{r} \right)^2 + \left(\frac{\partial u'_z}{\partial z} \right)^2 \right) + \left(r \frac{\partial (u'_\theta / r)}{\partial r} \right)^2 + \left(\frac{1}{r} \frac{\partial u'_r}{\partial \theta} \right)^2 + \left(\frac{1}{r} \frac{\partial u'_z}{\partial \theta} \right)^2 + \left(\frac{\partial u'_z}{\partial r} \right)^2 + \left(\frac{\partial u'_r}{\partial z} \right)^2 + \left(\frac{\partial u'_\theta}{\partial z} \right)^2 + 2 \left(\frac{\partial (u'_\theta / r)}{\partial r} \cdot \frac{\partial u'_r}{\partial \theta} + \frac{1}{r} \frac{\partial u'_\theta}{\partial z} \cdot \frac{\partial u'_z}{\partial \theta} + \frac{\partial u'_r}{\partial z} \cdot \frac{\partial u'_z}{\partial r} \right) \Bigg] \tag{3.8}$$

These magnitudes were also calculated in [5], however H.Singh and A.Prigent (2021) could not compute all the terms experimentally due to the fact that they had no access to the azimuthal coordinate. In our numerical case as we already explained all points in the grid are accessible, and therefore we are able to compute all the terms from expressions 3.6, 3.7 and 3.8. We averaged the radial profiles over the homogeneous directions $\hat{\theta}$ and $\hat{z}$ (the magnitudes u_α and derivatives $du_\alpha/d\gamma$ are not averaged in expressions 3.6, 3.7 and 3.8 to simplify the notation).

Furthermore, we were able to compute as well radial profiles for the production of kinetic energy $P = - < u'_\theta u'_r >_{\theta,z} (d < u_\theta >_{\theta,z} /dr - < u_\theta >_{\theta,z}$

$/r$), averaged over $\hat{\theta}$ and $\hat{z}$. Figure 3.13 presents the temporal evolution for the P profiles during 2 different time windows for $Re_o = 6500$. In **a** we have represented the k_{turb} temporal profiles at several radial positions in the gap. We defined two distinct temporal windows with vertical black lines in the subplot, the first window located in phase I of the process and the second window in phase II. For each window, we plotted several radial profiles of the production P, in **b** the profiles during phase I and in **c** the profiles during phase II. Both figures only show half of the gap ($0.5 < {}^{(r-r_i)}/_d < 1$) because in the inner half P is simply negligible. Hence, in **b** we can see that the production starts growing near the outer cylinder. These profiles correspond to phase I, when the vortical structures appear and grow until turbulence is reached. We observe also that rather than moving towards the inner cylinder, the maximum of production progressively gets closer to the outer wall, which is the opposite movement compared to the vortical structures behaviour. On the other hand, in subplot **c** we observe how the production decays with time, still the maximum being very close to the outer cylinder, corresponding to the turbulent free decay stage. Therefore, figure 3.13 confirms the idea that the production of kinetic energy in an abruptly stopped TC system will be located very close to the outer cylinder, the same place where turbulence is originated. Moreover, it confirms that phase I is defined by the generation of k while phase II corresponds to a progressive decay of turbulence.

Similarly to figure 3.13, in figure 3.14 we represented the evolution for the ε_{turb} radial profiles during phase I, in subplot **b**, and phase II, in subplot **c**. Subplot **a** shows the ε_{turb} temporal profiles at several positions in the gap for $Re_o = 6500$. Again and in the same way as for k_{turb}, we can identify three different phases during the simulation, with the same features: phase I shows how ε_{turb} increases drastically in a small period of time due to the generation of k_{turb} we have seen in figures 3.10 and 3.12; in phase II we observe how ε_{turb} decays with a pretty steady slope; finally, the slope of the decay changes, meaning the regime of the system is changing, in fact transitioning from a turbulent decay (phase II) to a viscous decay, corresponding to phase III. Now, in subplot **b** we observe how ε_{turb} progressively increases throughout the whole radial gap during phase I, with its maximum near the outer cylinder and gaining almost 5 orders of magnitude. In subplot **c** we can then see during phase II how ε_{turb} then starts decaying. The different times corresponding to the profiles have been listed in the same order spatially as the profile's maximums. That is, $t = 0.00318d^2/\nu$ corresponds to the blue profile, $t = 0.00405d^2/\nu$ to the orange one, and so on. However, it is very interesting to see that the dissipation progressively gets homogeneous over the gap. That is, we can see from $t = 0.00318d^2/\nu$ (blue profile) to $t = 0.01056d^2/\nu$ (purple profile) the ε_{turb} profiles become flatter, still with a maximum in the outer

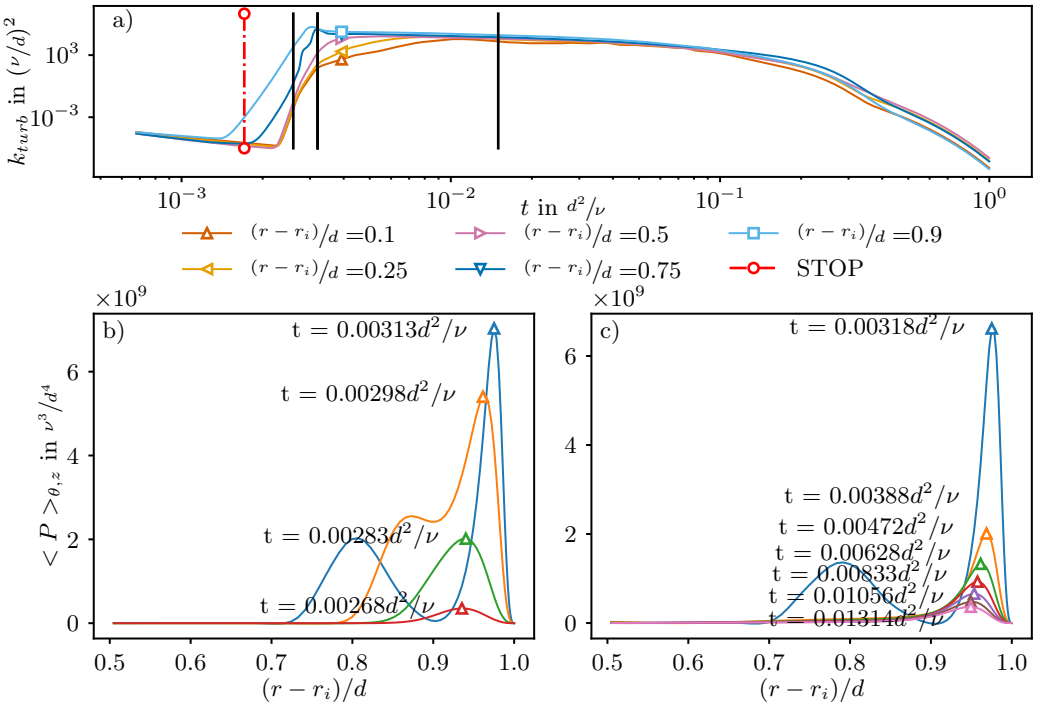

Figure 3.13: Production P temporal and radial profiles during generation and decay of turbulence for $Re_o = 6500$. **a)** Temporal profiles for different radial positions in the gap. **b)** Radial profiles during generation of turbulence (phase I). **c)** Radial profiles during decay of turbulence (phase II).

wall, and then the shape is maintained while decreasing in magnitude from $t = 0.01056d^2/\nu$ (purple profile) to $t = 0.01757d^2/\nu$ (pink profile). Hence, we can assume that the turbulent kinetic energy, and thus the turbulence, must also get more homogeneous in the gap during phase II. Such results agree with the idea that turbulence is generated near the outer cylinder and then progressively fills the whole gap between cylinders.

Proceeding in the same way as shown in figure 3.12, we fitted the ε_{turb} temporal profiles during phase II at different radial positions for several values of Re_o. We fitted the turbulent decay phase using a power-law function $\sim t^{\xi}$. The exponents we obtained are presented in table 3.5.

We observe once again the same tendency observed in table 3.4: near the outer cylinder, the exponents decrease when Re_o increases, meaning that ε_{turb} decays slower for higher values of Re_o.

Hence, we managed to characterise the free decay of turbulence by fitting both k_{turb} and ε_{turb} during their turbulent decay in phase II.

Nonetheless, we noticed that the numerical results we obtained regarding

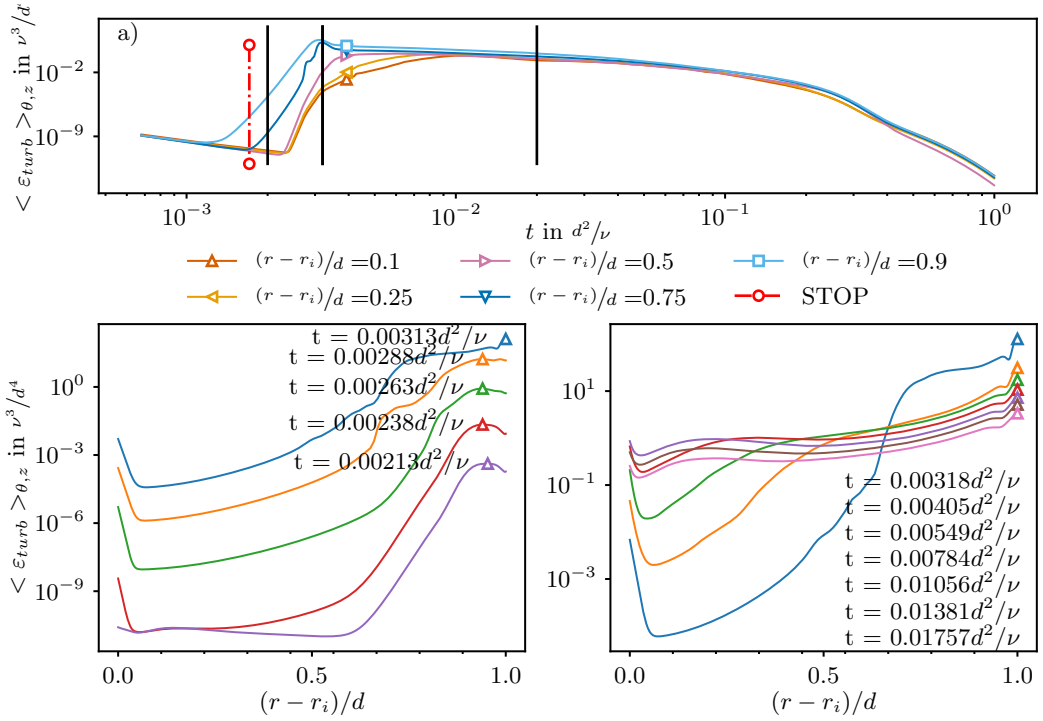

Figure 3.14: Turbulent decay rate ε_{turb} temporal and radial profiles during generation and decay of turbulence for Re_o = 6500. **a)** Temporal profiles for different radial positions in the gap. **b)** Radial profiles during generation of turbulence (phase I). **c)** Radial profiles during decay of turbulence (phase II).

Re_o	$(r - r_i)/\nu$	0.1	0.25	0.5	0.75	0.9
1700		-3.425	-3.459	-3.13	-3.25	-3.27
3000		-1.994	-2.187	-2.231	-2.17	-2.592
4400		-1.269	-1.576	-1.681	-1.726	-2.085
6500		-1.582	-1.691	-1.361	-1.354	-1.549

Table 3.5: Turbulent decay rate ε_{turb} power–law fitting exponents during the turbulent decay.

k and ε present a very important difference compared to the experimental results from [5]. In fact, H.Singh and A.Prigent (2021) were not able to fit the decay in phase II of neither magnitudes because both were oscillating too much during the turbulent decay, which they attributed to the constant reorganization of the vortices in the turbulent flow [5]. Such observation draw our attention towards the reason behind the lack of fluctuations in the profiles obtained numerically.

There exists some differences in the methodology used to obtain the results produced experimentally in [5] and those generated numerically in this document. In a first instance, as far as the computation of ε components is concerned, we were able to compute all the terms because we had access to the θ component. However, H.Singh and A.Prigent (2021) argued in [5] that such terms were actually negligible. Furthermore, when numerically computing derivatives we used a high order differentiation method which should be more accurate than the second-order central differencing approximation used experimentally in [5]. Also, the experimental profiles presented have been averaged spatially over z and in the a small region in the middle of the gap, and temporally over short time windows, taking 5 values before and after the instant for which the magnitudes are computed. Such process differs from our methodology, averaging just over θ and z. We wanted thereby to check if having access to the θ coordinate did actually enhanced our results, making them less fluctuating.

Then, figure 3.15 represents several temporal profiles for ε_{turb} at different radial locations in the gap for $Re_o = 3000$. The black profiles have been averaged over θ and z while the blue ones only over z. We observe that during phase I the profiles don't match for any of the 3 radial positions. However, we are more interested in phase II. We can see that except for subplot **a**, both profiles in **b** and **c** are quite identical. In subplot **a**, which corresponds to a position really close to the inner cylinder, we witness how the fluctuations in the blue profile become pretty significant and may lead to a erroneous fitting. Nonetheless, such variations don't compare to the oscillations reported in the experiments from [5]. Therefore, we are lead to think that the smoothness of the numerical results may be coming from the accuracy in the differentiation method.

3.3.3 Self–similarity

Based on the self–similarity criterion presented by Verschoof *et al.* (2016) [3], H. Singh and A. Prigent (2021) analysed in [5] the self–similar features for the azimuthal velocity radial profile $u_\theta(r)$ averaged axially and over time. Following the criterion, when the azimuthally averaged radial profiles $< u_\theta >_\theta$

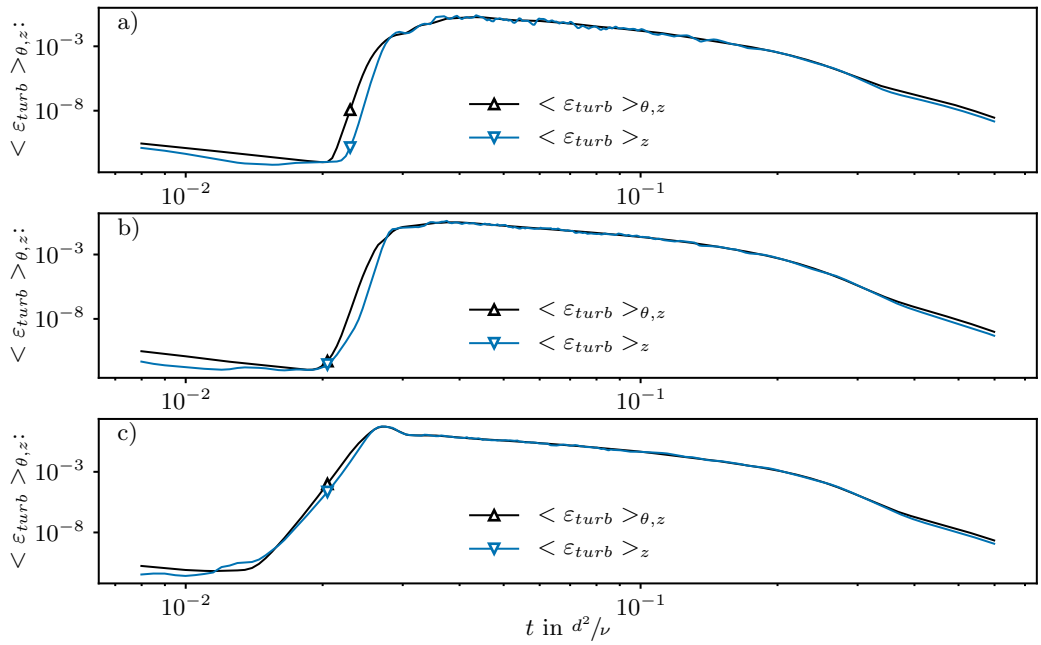

Figure 3.15: Turbulent decay rate ε_{turb} temporal profiles with and without averaging in the $\hat{\theta}$ direction for $Re_o = 3000$. Different radial positions in the gap are considered: **a)** $(r - r_i)/d = 0.1$; **b)** $(r - r_i)/d = 0.3$. **c)** $(r - r_i)/d = 0.8$.

are normalized respect to the spatial mean $< u_\theta >_{r,\theta,z}$, self–similarity in the profiles can be observed during the decay. Nonetheless, the results presented by H. Singh and A. Prigent concern the normalized profiles $< u_\theta >_{t,z}$ (averaged in time and axially). The results show that there is no complete self-similarity covering the whole decay process, but instead self–similarity of the profiles was observed during the second phase of the process, that is the turbulent decay period.

As foretold, in our case the temporal averaging is replaced by a spatial one in the homogeneous azimuthal direction, so that we are actually observing in figure 3.16 **b** the profiles for $< u_\theta >_{\theta,z} (r)/ < u_\theta >_{r,\theta,z}$.

Figure 3.16 is build out of two different subplots with $Re_o = 6500$. On the left, **a** presents the k_{turb} temporal profiles at different radial locations in the gap for $Re_o = 6500$. On such figure we defined two different temporal windows using vertical black lines. The first window $0.015 < t\nu/d^2 < 0.049$ is inside phase II (turbulent decay) while the second window $0.24 < t\nu/d^2 < 0.498$ belongs to phase III (viscous decay). In fact, **a** helps us identify which stage of the triphasic process we are looking at. On the other hand, on subplot **b** we plotted the radial profiles $< u_\theta >_{\theta,z} (r)/ < u_\theta >_{r,\theta,z}$ for both time windows defined earlier. We can clearly observe that the profiles exhibit

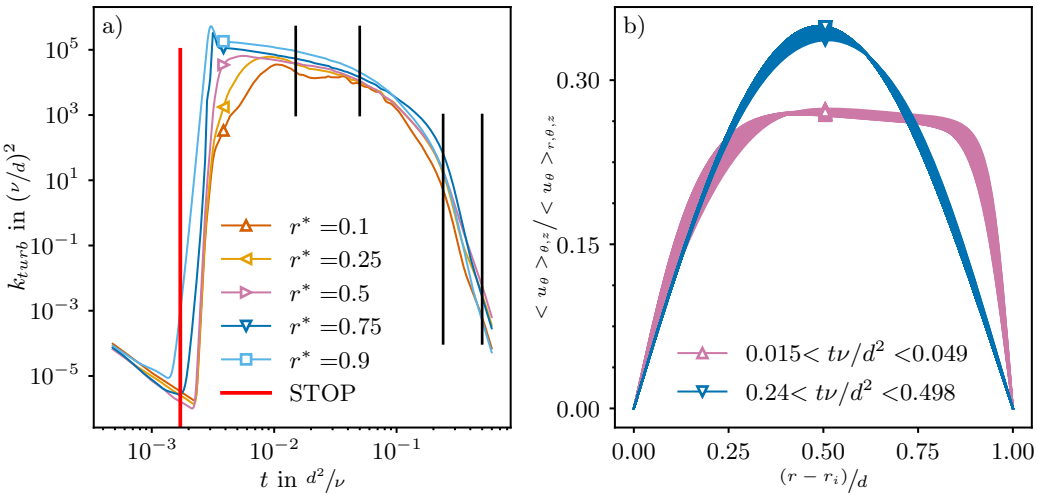

Figure 3.16: Self-similarity of $< u_\theta >_{\theta,z} (r)/ < u_\theta >_{r,\theta,z}$ radial profiles during the turbulent and viscous decay phases. In **a)** are represented different temporal profiles of the turbulent kinetic energy k_{turb} for different radial locations in the gap, whereas $r^* = {}^{(r-r_i)}/_d = 0.1,\ 0.25,\ 0.5,\ 0.75,\ 0.9$. The turbulent and the viscous decay phases have been windowed using vertical black lines, the turbulent decay being the one for $0.015d^2/\nu < t < 0.049d^2/\nu$ and the viscous decay for $0.24d^2/\nu < t < 0.498d^2/\nu$. In **b)** the radial profiles $< u_\theta >_{\theta,z} (r)/ < u_\theta >_{r,\theta,z}$ have been plotted for such temporal windows. $Re_o = 6500$

self-similarity in both windows. Furthermore, we have obtained the same results (qualitatively) for other values of Re_o. Therefore, it seems that the profiles are self-similar in both turbulent and viscous decay (phase I and II). We don't observe self-similarity neither during phase I nor during the transition from phase II to III.

4. Conclusions

In this study, the numerical results are presented for the abruptly stoppage of the outer cylinder of a Taylor–Couette system. This process triggers a triphasic phenomena where we observe generation and afterwards free decay of turbulence. The numerical results presented in this document are compared to the experimental outcomes for the same framework obtained by H.Singh and A.Prigent in their paper *Turbulence generation and decay in the Taylor–Couette system due to an abrupt stoppage* (2021) [5].

In a first instance, the flow is laminar while the outer cylinder is rotating at a constant Re_o. When Re_o drops to 0 abruptly, the azimuthal velocity in the outer wall also drops to 0 while remaining positive in the gap. Such configuration in the flow rapidly generates a centrifugal instability zone near the outer wall where small vortical structures start to generate and grow towards the inner cylinder. Shortly after the vortices fill the whole radial gap, the growth process being a competition between modes (number of pairs of vortices) translated into a continuous readjustment of the structures in the flow, the vortices are destabilised and the flow transitions to turbulence. Production of kinetic energy, turbulent kinetic energy and turbulent energy dissipation rate increase in the same region near the outer cylinder during this stage, which we named phase I in accordance with [5]. Then, after reaching a maximal value, the kinetic energy starts decaying. The whole turbulence in the flow decays freely as the system has no longer any energy input (both cylinders are static). This is phase II. Both turbulent kinetic energy and dissipation of turbulent kinetic energy radial profiles become flatter and progressively decay, meaning that turbulence has filled the whole gap and slowly crumbles. Such free decay of turbulence can be characterise by a power law function with its exponent dependant on the initial Re_o and the radial location in the gap.

Finally, the turbulence is replaced by large scale structures in the flow which evolves in a purely viscous decay. Self-similarity of the azimuthal velocity component can be observed during phases II and III.

Hence, we managed to reproduce numerically the triphasic phenomena observed experimentally in previous studies [5] and obtain the same Taylor–Couette flow behaviour. We analysed the centrifugal instability zone generated when the outer cylinder is abruptly stopped, responsible for the vortical structures that appear near the outer wall. We characterised the free decay of inhomogeneous and anisotropic turbulence by fitting both turbulent kinetic energy and turbulent kinetic energy dissipation rate according to a power law function, essential magnitudes for the $k - \varepsilon$ turbulence model. The decay exponents depend on the initial Re_o and on the radial position in the gap,

however a general tendency can be observed near the outer cylinder as Re_o increases.

Some results from this study also point towards the importance of the stopping time as parameter that may affect significantly the behaviour of the flow. Further research should focus on such observations.

Bibliography

[1] Peixinho, J.& Mullin, T. *Decay of turbulence in pipe flow.* Phys. Rev. Lett. 96, 094501. (2006)

[2] Touil, H., Bertoglio, J.-P. & Shao, L. *The decay of turbulence in a bounded domain.* J. Turbul. 3, N49. (2002)

[3] Verschoof, R.A., Huisman, S.G., Van der Veen, R.C.A., Sun, C. &Lohse, D. *Self-similar decay of high Reynolds number Taylor–Couette turbulence.* Phys. Rev. Fluids 1, 062402. (2016)

[4] Ostilla-Mónico, R., Zhu, X., Spandan, V., Verzicco, R. & Lohse, D., *Life stages of wall-bounded decay of Taylor–Couette turbulence.* Phys. Rev. Fluids 2, 114601. (2017)

[5] H. Singh, A. Prigent *Turbulence generation and decay in the Taylor–Couette system due to an abrupt stoppage* J. Fluid Mech., vol. 918 (2021)

[6] Kaiser, F., Frohnappel, B., Ostilla-Mónico, R., Kriegseis, J., Rival, D.E. & Gatti, D. *On the stages of vortex decay in an impulsively stopped, rotating cylinder.* J. Fluid Mech. 885, A6. (2020)

[7] Jose Manuel López, Daniel Feldmann, Markus Rampp, Alberto Vela-Martín, Liang Shi, Marc Avila *nsCouette – A high-performance code for direct numerical simulations of turbulent Taylor–Couette flow*, SoftwareX 11 100395 (2020)

[8] Guseva A, Willis AP, Hollerbach R, Avila M. *Transition to magnetorotational turbulence in Taylor–Couette flow with imposed azimuthal magnetic field.* New J Phys ;17(9). 093018. (2015)

[9] Shi L, Rampp M, Hof B, Avila M. *A hybrid MPI-OpenMP parallel implementation for pseudospectral simulations with application to Taylor–Couette flow.* Comput & Fluids;106:1–11. (2015)

[10] Grossmann S., Lohse D. and Sun C. *High-Reynolds number Taylor–Couette turbulence*, Annu Rev Fluid Mech ;48(1):53–80 (2016)